Alma Mater Studiorum · Università di Bologna

**SCUOLA DI SCIENZE**
**Corso di Laurea Magistrale in Fisica**

# Investigation of spectral stability of X-ray tubes by simulations and experimental spectrum measurements

**Tesi di Laurea in Fisica**

**Relatore:**
Chiar.mo
Giuseppe Baldazzi

**Presentata da:**
**Riccardo Baldoni**

**Correlatore:**
Dott. Gereon Vogtmeier
Dott. Klaus Juergen Engel

**III Sessione**
**Anno Accademico 2014/2015**

Yesterday is gone. Tomorrow has not yet come. We have only today. Let us begin.

— Mother Teresa

**To my mother**
**and my father**

# Contents

# List of Figures

# List of Tables

# Abstract It

L'obiettivo di questo lavoro è quello di analizzare la stabilità di uno spettro raggi X emesso da un tubo usurato per analisi cardiovascolari, in modo da verificare il suo comportamento. Successivamente questo tipo di analisi sarà effettuata su tubi CT. Per raggiungere questo scopo è stato assemblato un particolare set-up con un rivelatore al germanio criogenico in modo da avere la miglior risoluzione energetica possibile ed alcuni particolari collimatori così da ridurre il flusso fotonico per evitare effetti di pile-up. Il set-up è stato costruito in modo da avere il miglior allineamento possibile nel modo più veloce possibile, e con l'obiettivo di rendere l'intero sistema portabile. Il tubo usato è un SRM Philips tube per analisi cardiovascolari; questa scelta è stata fatta in modo da ridurre al minimo i fattori esterni (ottica elettromagnetica, emettitori) e concentrare l'attenzione solo sugli effetti, causati dalle varie esposizioni, sull'anodo (roughness e bending) e sul comportamento di essi durante il surriscaldamento e successivo raffreddamento del tubo. I risultati mostrano come durante un'esposizione alcuni fattori di usura del tubo possono influire in maniera sostanziale sullo spettro ottenuto e quindi alterare il risultato. Successivamente, nell'elaborato, mediante il software Philips di ricostruzione e simulazione dello spettro si è cercato di riprodurre, variando alcuni parametri, la differenza riscontrata sperimentalmente in modo da poter simulare l'instabilità e correggere i fattori che la causano. I risultati sono interessanti non solo per questo esperimento ma anche in ottica futura, per lo sviluppo di applicazioni come la spectral CT. Il passo successivo sarà quello di spostare l'attenzione su un CT tube e verificare se l'instabilità riscontrata in questo lavoro è persiste anche in una analisi più complessa come quella CT.

# Abstract En

The goal of this work is the investigation of the X-ray spectrum stability from a normal cardiovascular X-ray tube (not a CT tube) with an aged anode, so that all variations of the spectrum can be analyzed with quantitative measurements and the influence of the performance could be estimated, for future application like spectral CT. These variations can then be modelled to be included in simulation tools. To reach this results an energy resolving photon counting direct conversion detector made from Germanium was used, in order to have the best energy resolution and some special

tungsten collimators were used to reduce the high flux. The design of the set-up allows for a freely definable orientation with respect to the X-ray focal spot emission area and the relocation of the whole system in a different laboratory. This normal SRM tube was chosen to start measurements with a simple setup and avoid additional influences from electron optics and other tube components that are integrated in high end CT tubes for example. The aim was to try to analyse only the changing in life time, like anode ageing (roughness, crack and bending) and its behaviour during the heating and cooling. The designed modular set-up can be used in a very flexible way also for the investigation of other X-ray tubes. As follow up it would be interesting to validate the measured effects also in other X-ray tubes and to confirm the quantitative results that have been calculated in this study.

# Introduction

X-rays are widely used in medicine and one of the main applications is diagnostic radiography. More particular applications are CT and spectral CT, interventional X-ray imaging, diagnostic imaging with high resolution, fluoroscopy and many more and other mainstream usages of X-ray are security scanning, material analysis, crack searching and others. The photon spectrum produced by an X-ray set is a complicated function that depends on many factors: the type of tube and target material, the accelerating potential, and the inherent and added filtration which modifies the primary beam. In the Chapter 1 all these factors will be explained and analysed. For many diagnostic equipments, the high voltage supply changes with the tube current and it is difficult to specify these changes precisely. A measurement of the diagnostic spectrum is therefore desirable to ensure that the correct operating conditions are chosen for a particular application. Knowledge of the X-ray diagnostic beam is also required to reach protocol optimization and reduce patient dose (especially in CT scans where the exposure is very high) and at the same time, to find a compromise to improve image quality while still reducing the dose. While the theory about the physics of X-ray generation is already well-known, in practice severe (and even history-dependent) variations of an "X-ray spectrum" are observed. On the other hand, with the growth of new applications more and more precise information on the generation of the spectrum and the spectrum itself is required.
Peaple and Burt have used scintillation spectrometers to measure the photon spectrum [19]. Measurements of medical diagnostic X-ray spectra have been reported by several authors, using different detectors: NaI(Tl) (Epp and Weiss, 1966 [10]), Ge(Li) or Si(Li) (Seelentag and Panzer, 1979; O'Foghludha and Johnson, 1981), and surface barrier detectors (Pani et al., 1987). A comparison reveals large differences amongst the spectra obtained with such detectors. Ge or Si (L1) have been more frequently used for accurate spectral measurements, with proper corrections (Fewell and Shuping, 1977; Seelentag and Panzer, 1979). However, there are some disadvantages in using these systems: in measurements with medical X-ray equipment, it is necessary to decrease the count rate (later during the thesis this will be explained) and reduce the thermal noise of the detector by cooling. With the used setups it is impossible to measure photons with different incident angles simultaneously, and hence, scattered radiation. The methods used to align the systems were often complicated and the complete spectrometers could not be readily applied to measurements on different types of set in other locations.
Recently there have been improvements in the quality of radiology systems: these improvements regard in particular the detector system (flat-panel, multi-slices detectors) and the digital image elaboration systems. However this technological development does not correspond to an equal improvement in radiogenic sources knowledge. Of course, some general aspects, like angular dependence are known, but to date, with

the development of new applications sensitive to the X-ray spectrum like e.g. spectral CT, more precise knowledges is now necessary. Aspects such as the stability of the spectrum during an examinations, have always been overlooked, but now with the development of new techniques, a better knowledge and more details are required. It is very difficult to measure an X-ray spectrum due to the fact that many experimental effects produce artifacts which are in particular difficult (or due to lack of knowledge even impossible) to correct for. At the moment it is not known how much a measured spectrum corresponds to reality and for this reason even trying to simulate the spectra is difficult. The main problem is that the existing theories and simulation tools are sufficient when only general knowledge of the spectrum is required. For applications with integrating detectors, the provided theoretical spectra are good enough, but becomes insufficient when more accurate information as shown in the list below is required. However some effects can be simulated with these tools and this study will also provide more information on this subject. An attempt will be made to model the effects found, create models for them, and use these models with the existing tools to calculate the spectrum generated more accurately. Especially in CT diagnostics, one of the main factors that influences the ability of the radiologist to detect subtle lesions in X-ray-based images is the signal-to-noise ratio provoked by the lesion in the image. This important factor ultimately depends on the spectrum of the X-ray beam which passes through the patient during the procedure. For this precise reason it is necessary to have a deeper understanding of factors already known to influence and determine a different kind of spectrum emitted by the tube. The most important effects are listed below:

- the ageing of the anode and its consequent roughness
- heating and cooling of the anode during a working day and its effect on the anode surface topology (e.g. bending and surface curvature);
- the Heel effect (we will see all the two dimensional effect);
- the gravity force to which the X-Tube is subjected;
- generator stability (ripple and rising and falling edge).

Of course it is impossible to separate and analyse all factors and their influence. In our studies we have tried to assess as many as possible and analyse how these affect the spectrum, in order to have a better understanding of the spectrum, which will be beneficial both for the techniques used and for the patients.
In these studies a mobile unit with precise collimators positioning, beam shielding and position detection was developed to investigate spectral distribution and stability of the X-ray source and to carry out quantitative analysis. The collimating system and the whole set-up was designed so that the setting up and alignment procedure was relatively quick and simple. Strong beam collimation was necessary because the flux that is reliable analyzable by the counting detector was around 5 order of magnitude below the tube flux (effect explained in detail in later chapters). Without taking this effect into account, the spectrum could be modified by the pile-up events in the detector and which make it impossible to interpret the spectrum obtained. To avoid this, there are some ways of decreasing the flux and the most significant are:

- collimation
- filtering

The problem of filtering is that low-energy photons are filtered much stronger than high-energy photons and an additional effect like scattering inside the material can modify the end results. Therefore the best solution is collimation, but here there are alignment problems. Certainly another solution would be to reduce mA loaded to acquire the spectrum, but in this way the spectrum acquired would no longer represent the operating conditions of CT examinations and the problem of heat-induced topology changes of the anode surface would not be taken into account. For these reasons the tests were done using only collimators and positioning the detector as far from the tube as possible. In the following paragraphs all the problems related to the building of the set-up and how they were solved will be explained (reducing high flux, distance and collimation). Moreover the set-up was designed to make the alignment of the collimators, the X-ray beam and the detector as simple and as fast as possible, so that the system could be used with different tubes. For this procedure, a flat panel detector was used to understand beam collimation and X-ray spot geometry and to align the two used collimators with respect to X-ray spot and detection area. With the present collimating system, measurements of the unfiltered spectra from diagnostic sets were restricted to low tube currents.
This analysis is important for Philips because it provides a better understanding of how the spectrum is generated and how the above factors contribute to this. If the spectrum can not be reproduced for unknown reasons, and changes randomly, the problem is more serious because a systematic correction can not be found. The main interest for Philips is:

1. Quantification of dynamic changes of the spectrum
2. Understanding of the origins of dynamical spectrum changes
3. Understanding of "static" effects, like e.g. surface roughness.

Some information has been available for decades, but now more detailed information is necessary due to further development and Philips desire to enter the field of the spectral CT. The spectral CT, the latest technology of this kind, is based on the spectrum knowledge, which allows e.g. for material separation, like e.g. of bone mineral, tissues, and contrast agent(s). In this operating mode the spectrally resolved X-ray attenuation has to be measured assuming a reference spectrum. If it is possible to identify the factors that influence the input spectrum and to what extent, it would be possible to forecast the input spectrum with higher accuracy and therefore enable a more accurate spectral analysis of the image content.
The initial results got in this work already represent an interesting finding. Knowing the stability of the spectrum in a working day or for the tube life expectancy, will provide Philips with more precise date for their customers on how frequently they require calibration, and how frequently the tube needs to be replaced. From the result got in this work, it is evident that the tube temperature rises but until now this has never been taken into consideration. The purpose in this work, is to record all possible effects in order to be able to check and compare them with other experiments and other CT tubes.

# Chapter 1

# Historical and theoretical features

In this chapter some theoretical and historical features were described. To do this some books and articles are used to guide us along this path. [13] [7]

## 1.1 Historical Approaches to Diagnosis

In the 1800s and before, physicians were extremely limited in their ability to obtain information about the illnesses and injuries of patients. They relied essentially on the five human senses, and what they could not see, hear, feel, smell, or taste usually went undetected. Even these senses could not be exploited fully, because patient modesty and the need to control infectious diseases often prevented full examination of the patient. Frequently, physicians served more to reassure the patient and comfort the family rather than to intercede in the progression of illness or facilitate recovery from injury. More often than not, fate was more instrumental than the physician in determining the course of a disease or injury. The twentieth century witnessed remarkable changes in the physician's ability to intervene actively on behalf of the patient. These changes dramatically improved the health of humankind around the world.


**Figure 1.1:** *Computed tomography.*

Diagnostic medicine has improved dramatically, and therapies have evolved for cure

or maintenance of persons with a variety of maladies. Diagnostic probes to identify and characterize problems in the internal anatomy and physiology of patients have been a major contribution to these improvements. By far, X-rays are the most significant of these diagnostic probes. Diagnostic X-ray studies have been instrumental in moving the physician into the role of an active intervener in disease and injury and a major influence on the prognosis for recovery.

**Capsule History of Medical Imaging** In November 1895 Wilhelm Röntgen, a physicist at the University of Würzburg, was experimenting with cathode rays. These rays were obtained by applying a potential difference across a partially evacuated glass "discharge" tube. Röntgen observed the emission of light from crystals of barium platinocyanide some distance away, and he recognized that the fluorescence had to be caused by radiation produced by his experiments. He called the radiation "X-rays" and quickly discovered that the new radiation could penetrate various materials and could be recorded on photographic plates. Among the more dramatic illustrations of these properties was a radiograph of a hand (Fig. 1.2) that Röntgen included in early presentations of his findings. This radiograph captured the imagination of both scientists and the public around the world. Within a month of their discovery, X-rays were being explored as medical tools in several countries, including Germany, England, France, and the United States. In 1901, Röntgen was awarded the first Nobel Prize in Physics.

**Figure 1.2:** *A radiograph of the hand taken by Röntgen in December 1895. His wife may have been the subject.*

Two months after Röntgen's discovery, Poincaré demonstrated to the French Academy of Sciences that X-rays were released when cathode rays struck the wall of a

gas discharge tube. Shortly thereafter, Becquerel discovered that potassium uranyl sulfate spontaneously emitted a type of radiation that he termed Becquerel rays, now popularly known as $\beta$-particles. Marie Curie explored Becquerel rays for her doctoral thesis and chemically separated a number of elements. She discovered the radioactive properties of naturally occurring thorium, radium, and polonium, all of which emit $\alpha$-particles, a new type of radiation. In 1900, $\gamma$ rays were identified by Villard as a third form of radiation. In the meantime, J.J.Thomson reported in 1897 that the cathode rays used to produce X-rays were negatively charged particles (electrons) with about 1/2000 the mass of the hydrogen atom. In a period of 5 years from the discovery of x rays, electrons and natural radioactivity had also been identified, and several sources and properties of the latter had been characterized. Over the first half of the twentieth century, X-ray imaging advanced with the help of improvements such as intensifying screens, hot-cathode X-ray tubes, rotating anodes, image intensifiers, and contrast agents. In addition, X-ray imaging was joined by other imaging techniques that employed radioactive nuclides and ultrasound beams as radiation sources for imaging. Through the 1950s and 1960s, diagnostic imaging progressed as a coalescence of X-ray imaging with the emerging specialties of nuclear medicine and ultrasonography. This coalescence reflected the intellectual creativity nurtured by the synthesis of basic science, principally physics, with clinical medicine.

## 1.2 Interaction of Radiation with Matter

In a radiation interaction, the radiation and the material with which it interacts may be considered as a single system. When the system is compared before and after the interaction, certain quantities will be found to be invariant. Invariant quantities are exactly the same before and after the interaction. Invariant quantities are said to be conserved in the interaction. One quantity that is always conserved in an interaction is the total energy of the system, with the understanding that mass is a form of energy. Other quantities that are conserved include momentum and electric charge. Some quantities are not always conserved during an interaction. For example, the number of particles may not be conserved because particles may be fragmented, fused, "created" (energy converted to mass), or "destroyed" (mass converted to energy) during an interaction. Interactions may be classified as either elastic or inelastic. An interaction is elastic if the sum of the kinetic energies of the interacting entities is conserved during the interaction. If some energy is used to free an electron or nucleon from a bound state, kinetic energy is not conserved and the interaction is inelastic. Total energy is conserved in all interactions, but kinetic energy is conserved only in interactions designated as elastic.

### 1.2.1 Exitation, Ionization, and Radiative Losses

Energetic charged particles all interact with matter by electrical (i.e., coulombic) forces and lose kinetic energy via excitation, ionization, and radiative losses. Excitation and ionization occur when charged particles lose energy by interacting with orbital electrons. Excitation is the transfer of some of the incident particle's energy to electrons in the absorbing material, promoting them to electron orbitals farther from the nucleus (i.e., higher energy levels). In excitation, the energy transferred to an electron does not exceed its binding energy. Following excitation, the electron will return to a lower energy level, with the emission of the excitation energy in the form of electromagnetic radiation

or Auger electrons. This process is referred to as de-excitation. If the transferred energy exceeds the binding energy of the electron, ionization occurs, whereby the electron is ejected from the atom. The result of ionization is an ion pair consisting of the ejected electron and the positively charged atom. Sometimes the ejected electrons possess sufficient energy to produce further ionizations called secondary ionization. These electrons are called delta rays. Approximately 70% of charged particle energy deposition leads to non-ionizing excitation.

### Specific Ionization

Specific ionization increases with the electrical charge of the particle and decreases with incident particle velocity. A larger charge produces a greater coulombic field; as the particle loses energy, it slows down, allowing the coulombic field to interact at a given location for a longer period of time. As the alpha particle slows, the specific ionization increases to a maximum (called the Bragg peak), beyond which it decreases rapidly as the alpha particle picks up electrons and becomes electrically neutral, thus losing its capacity for further ionization. The large Bragg peak associated with heavy charged particles has medical applications in radiation therapy.

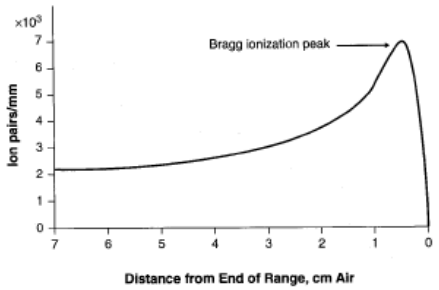


**Figure 1.3:** *Specific ionization (ion pairs/mm) as a function of distance from the end of range in air for a 7.69-MeV alpha particle from polonium 214 (Po214). Rapid increase in specific ionization reaches a maximum (Bragg peak) and then drops off sharply as the particle kinetic energy is exhausted and the charged particle is neutralized.*

By adjusting the kinetic energy of heavy charged particles, a large radiation dose can be delivered at a particular depth and over a fairly narrow range of tissue containing a lesion. On either side of the Bragg peak, the dose to tissue is substantially lower. Heavy particle accelerators are used at some medical facilities to provide this treatment in lieu of surgical excision or conventional radiation therapy.

### Charged Particle Tracks

Another important distinction between heavy charged particles and electrons is their paths in matter. Electrons follow tortuous paths in matter as the result of multiple scattering events caused by coulombic deflections (repulsion and/or attraction). The sparse non-uniform ionization track of an electron is shown in Fig. 1.4. On the other hand, the larger mass of a heavy charged particle results in a dense and usually linear ionization track Fig. 1.4. The path length of a particle is defined as the actual distance the particle travels. The range of a particle is defined as the actual depth of penetration of the particle in matter. As illustrated in Fig. 1.4, the path length of the electron

almost always exceeds its range, whereas the straight ionization track of a heavy charged particle results in the path and range being nearly equal.

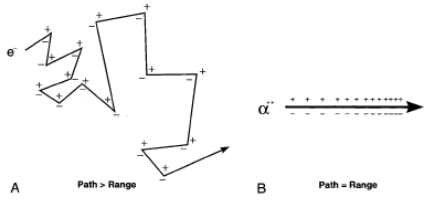


**Figure 1.4:** *A: Electron scattering results in the path length of the electron being greater than its range. B: Heavily charged particles, like alpha particles, produce a dense nearly linear ionization track, resulting in the path and range being essentially equal.*

### Linear Energy Transfer

The amount of energy deposited per unit path length is called the linear energy transfer (LET) and is usually expressed in units of eV/cm. The LET of a charged particle is proportional to the square of the charge and inversely proportional to the particle's kinetic energy. LET is the product of specific ionization (IP/cm) and the average energy deposited per ion pair (eV/IP). The LET of a particular type of radiation describes the energy deposition density, which largely determines the biologic consequence of radiation exposure. In general, "high LET" radiations (alpha particles, protons, etc.) are much more damaging to tissue than "low LET" radiations, which include electrons (e-, -, and W) and ionizing electromagnetic radiation (gamma and X-rays, whose interactions set electrons into motion).

### Scattering

Scattering refers to an interaction resulting in the deflection of a particle or photon from its original trajectory. A scattering event in which the total kinetic energy of the colliding particles is unchanged is called elastic. Billiard ball collisions, for example, are elastic (disregarding frictional losses). When scattering occurs with a loss of kinetic energy, the interaction is said to be inelastic. For example, the process of ionization can be considered an elastic interaction if the binding energy of the electron is negligible compared to the kinetic energy of the incident electron. If the binding energy that must be overcome to ionize the atom is significant, the process is said to be inelastic.

### Radiative Interactions - Bremsstrhlung

Electrons can undergo inelastic interactions with atomic nuclei in which the path of the electron is deflected by the positively charged nucleus, with a loss of kinetic energy. This energy is instantaneously emitted as ionizing electromagnetic radiation (X-ray). The energy of the X-ray is equal to the energy lost by the electron, as required by the conservation of energy. The radiation emission accompanying electron deceleration is called bremsstrahlung, a German word meaning "braking radiation" (Fig. 1.5).

The deceleration of the high-speed electrons in an X-ray tube produces the bremsstrahlung X-rays used in diagnostic imaging. When the kinetic energy of the electron is low, the bremsstrahlung photons are emitted predominantly between the

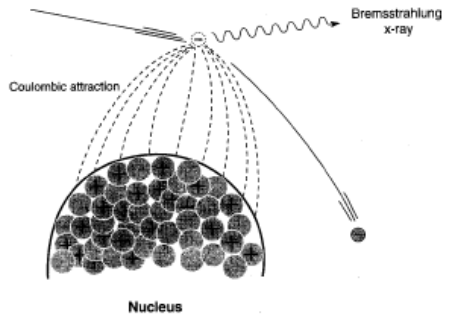


**Figure 1.5:** *Radiative energy loss via bremsstrhlung (braking radiation).*

angles of 60 and 90 degrees relative to the incident electron trajectory. At higher electron kinetic energies, the X-rays tend to be emitted in the forward direction. The probability of bremsstrahlung emission per atom is proportional to Z2 of the absorber. Energy emission via bremsstrahlung varies inversely with the square of the mass of the incident particle. Therefore, protons and alpha particles will produce less than one-millionth the amount of bremsstrahlung radiation as electrons of the same energy. The ratio of electron energy loss by bremsstrahlung production to that lost by excitation and ionization can be calculated from Equation 1.1:

$$\frac{BremsstrahlungRadiation}{ExcitationandIonization} = \frac{E_k Z}{820} \tag{1.1}$$

where $E_k$ is the kinetic energy of the incident electron in MeV; and Z is the atomic number of the absorber. Bremsstrahlung X-ray production accounts for approximately 1% of the energy loss when electrons are accelerated to an energy of 100 keV and collide with a tungsten (Z = 74) target in an X-ray tube.

## 1.3 X- and Gamma-Ray Interaction

When traversing matter, photons will penetrate, scatter, or be absorbed. There are four major types of interactions of X- and Gamma-ray photons with matter, the first three of which play a role in diagnostic radiology and nuclear medicine: (a) Rayleigh scattering, (b) Compton scattering, (c) photoelectric absorption, and (d) pair production.

### 1.3.1 Rayleigh scattering

In Rayleigh scattering, the incident photon interacts with and excites the total atom, as opposed to individual electrons as in Compton scattering or the photoelectric effect. This interaction occurs mainly with very low energy diagnostic X-rays, as used in mammography (15 to 30 keV). During the Rayleigh scattering event, the electric field of the incident photon's electromagnetic wave expends energy, causing all of the electrons in the scattering atom to oscillate in phase. The atom's electron cloud immediately radiates this energy, emitting a photon of the same energy but in a slightly different direction (Fig. 1.6). In this interaction, electrons are not ejected and thus ionization does not occur. In general, the scattering angle increases as the X-ray energy decreases. In medical imaging, detection of the scattered X-ray will have a deleterious

effect on image quality. However, this type of interaction has a low probability of occurrence in the diagnostic energy range. In soft tissue, Rayleigh scattering accounts for less than 5% of X-ray interactions above 70 keV and at most only accounts for 12% of interactions at approximately 30 keV. Rayleigh interactions are also referred to as "coherent" or "classical" scattering.

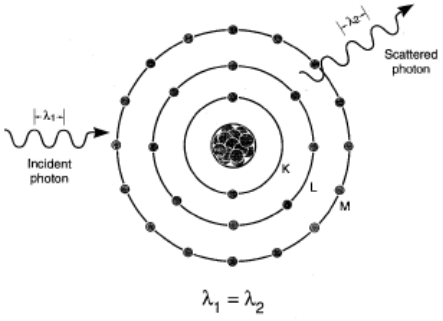


**Figure 1.6:** *Rayleigh scattering. Diagram shows the incident photon $\lambda_1$ interacts with an atom and the scattered photon $\lambda_2$ is being emitted with approximately the same wavelength and energy. Rayleigh scattered photons are typically emitted in the forward direction fairly close to the trajectory of the incident photon. K, L, and M are electron shells.*

### 1.3.2 Compton scattering

Compton scattering (also called inelastic) is the predominant interaction of X-ray and Gamma-ray photons in the diagnostic energy range with soft tissue. In fact, Compton scattering not only predominates in the diagnostic energy range above 26 keV in soft tissue, but continues to predominate well beyond diagnostic energies to approximately 30 MeV. This interaction is most likely to occur between photons and outer ("valence") shell electrons (Fig. 1.7). The electron is ejected from the atom, and the photon is scattered with some reduction in energy. As with all types of interactions, both energy and momentum must be conserved. Thus the energy of the incident photon ($E_0$) is equal to the sum of the energy of the scattered photon ($E_{sc}$) and the kinetic energy of the ejected electron ($E_{e-}$), as shown in Equation.

$$E_0 = E_{sc} + E_{e-} \tag{1.2}$$

The binding energy of the electron that was ejected is comparatively small and can be ignored.

Compton scattering results in the ionization of the atom and a division of the incident photon energy between the scattered photon and ejected electron. The ejected electron will lose its kinetic energy via excitation and ionization of atoms in the surrounding material. The Compton scattered photon may traverse the medium without interaction or may undergo subsequent interactions such as Compton scattering, photoelectric absorption, or Rayleigh scattering. The energy of the scattered photon can be calculated from the energy of the incident photon and the angle of the scattered photon (with respect to the incident trajectory):

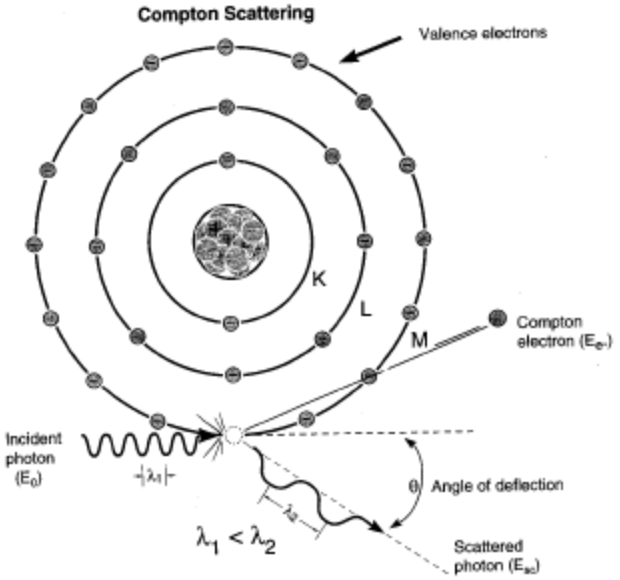


**Figure 1.7:** *Compton scattering. Diagram shows the incident photon with energy $E_0$, interacting with a valence shell electron that results in the ejection of the Compton electron ($E_{e^-}$) and the simultaneous emission of a Compton scattered photon $E_{sc}$ emerging at an angle e relative to the trajectory of the incident photon. K, L, and M are electron shells.*

$$E_{sc} = \frac{E_0}{1 + \frac{E_0}{511keV}(1 - cos\theta)} \tag{1.3}$$

where $E_{sc}$ = energy of the scattered photon,
$E_0$ = the incident photon energy, and
$\theta$ = the angle of the scattered photon.

As the incident photon energy increases, both scattered photons and electrons are scattered more toward the forward direction. In X-ray transmission imaging, these photons are much more likely to be detected by the image receptor, thus reducing image contrast. In addition, for a given scattering angle, the fraction of energy transferred to the scattered photon decreases with increasing incident photon energy. Thus, for higher energy incident photons, the majority of the energy is transferred to the scattered electron. When Compton scattering does occur at the lower X-ray energies used in diagnostic imaging (18 to 150 keV), the majority of the incident photon energy is transferred to the scattered photon, which, if detected by the image receptor, contributes to image degradation by reducing the primary photon attenuation differences of the tissues. The laws of conservation of energy and momentum place limits on both scattering angle and energy transfer. In fact, the maximal energy of the scattered photon is limited to 511 keV at 90 degrees scattering and to 255 keV for a 180-degree scattering (backscatter) event. These limits on scattered photon energy hold even for extremely high-energy photons. The scattering angle of the ejected electron cannot exceed 90 degrees, whereas that of the scattered photon can be any value including a 180-degree backscatter. In contrast to the scattered photon, the energy of the ejected electron is usually absorbed near the scattering site. The

incident photon energy must be substantially greater than the electron's binding energy before a Compton interaction is likely to take place. Thus, the probability of a Compton interaction increases, compared to Rayleigh scattering or photoelectric absorption, as the incident photon energy increases. The probability of Compton interaction also depends on the electron density (number of electrons/g per density). With the exception of hydrogen, the total number of electrons/g is fairly constant in tissue; thus, the probability of Compton scattering per unit mass is nearly independent of Z, and the probability of Compton scattering per unit volume is approximately proportional to the density of the material. Compared to other elements, the absence of neutrons in the hydrogen atom results in an approximate doubling of electron density. Thus, hydrogenous materials have a higher probability of Compton scattering than a non-hydrogenous material of equal mass.

### 1.3.3 Photoelectric effect

In the photoelectric effect, all of the incident photon energy is transferred to an electron, which is ejected from the atom. The kinetic energy of the ejected photoelectron ($E_e$) is equal to the incident photon energy ($E_0$) minus the binding energy of the orbital electron ($E_b$) (Fig 1.8). In order for photoelectric absorption to occur, the incident photon energy must be greater than or equal to the binding energy of the electron that is ejected. The ejected electron is most likely one whose binding energy is closest to, but less than, the incident photon energy. Following a photoelectric interaction, the atom is ionized, with an inner shell electron vacancy. This vacancy will be filled by an electron from a shell with a lower binding energy. This creates another vacancy, which, in turn, is filled by an electron from an even lower binding energy shell. Thus, an electron cascade from outer to inner shells occurs. The difference in binding energy is released as either characteristic X-rays or auger electrons. The probability of characteristic X-ray emission decreases as the atomic number of the absorber decreases and thus does not occur frequently for diagnostic energy photon interactions in soft tissue. The probability of photoelectric absorption per unit mass is approximately proportional to $Z^3/E^3$, where Z is the atomic number and E is the energy of the incident photon.

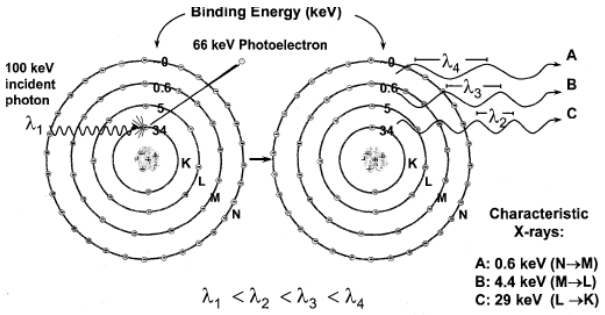


**Figure 1.8:** *Photoelectric absorption. Left: Diagram shows a 100-keV photon is undergoing photoelectric absorption with an iodine atom. In this case, the K-shell electron is ejected with a kinetic energy equal to the difference between the incident photon energy and the K-shell binding energy of 34 or 66 keV. Right: The vacancy created in the K shell results in the transition of an electron from the L shell to the K shell. This electron cascade will continue resulting in the production of other characteristic x-rays of lower energies. Note that the sum of the characteristic x-ray energies equals the binding energy of the ejected photoelectrons.*

The benefit of photoelectric absorption in X-ray transmission imaging is that there are no additional non-primary photons to degrade the image. The fact that the probability of photoelectric interaction is proportional to $1/E_3$ explains, in part, why image contrast decreases when higher X-ray energies are used in the imaging process. Although the probability of the photoelectric effect decreases, in general, with increasing photon energy, there is an exception. For every element, a graph of the probability of the photoelectric effect, as a function of photon energy, exhibits sharp discontinuities called absorption edges. The probability of interaction for photons of energy just above an absorption edge is much greater than that of photons of energy slightly below the edge. As mentioned above, a photon cannot undergo a photoelectric interaction with an electron in a particular atomic shell or subshell if the photon's energy is less than the binding energy of that shell or subshell. This causes the dramatic decrease in the probability of photoelectric absorption for photons whose energies are just below the binding energy of a shell. Thus, the photon energy corresponding to an absorption edge is the binding energy of the electrons in that particular shell or subshell. The photon energy corresponding to a particular absorption edge increases with the atomic number (Z) of the element. At photon energies below 50 keV the photoelectric effect plays an important role in imaging soft tissue. The photoelectric absorption process can be used to amplify differences in attenuation between tissues with slightly different atomic numbers, thereby improving image contrast. This differential absorption is exploited to improve image contrast in the selection of X-ray tube target material and filters in *mammography*. The photoelectric process predominates when lower energy photons interact with high Z materials. In fact, photoelectric absorption is the primary mode of interaction of diagnostic X-rays with screen phosphors, radiographic contrast materials, and bone. Conversely, Compton scattering will predominate at most diagnostic photon energies in materials of lower atomic number such as tissue and air.

### 1.3.4 Pair production

Pair production can only occur when the energies of X- and Gamma rays exceed 1.02 MeV. In pair production, an X- or Gamma ray interacts with the electric field of the nucleus of an atom. The photon's energy is transformed into an electron-positron pair. The rest mass energy equivalent of each electron is 0.511 MeV and this is why the energy threshold for this reaction is 1.02 MeV. Photon energy in excess of this threshold is imparted to the electrons as kinetic energy. The electron and positron lose their kinetic energy via excitation and ionization. As discussed previously, when the positron comes to rest, it interacts with a negatively charged electron, resulting in the formation of two oppositely directed 0.511 MeV annihilation photons. Pair production is of no consequence in diagnostic X-ray imaging because of the extremely high energies required for it to occur. In fact, pair production does not become significant unless the photon energies greatly exceed the 1.02 MeV energy threshold.

## 1.4 Radiation quantity and quality

X-rays are used for medical applications and for X-ray imaging thanks to the ability of some structures of the body to absorb or let through a part of them. Below are listed all the physical aspects that allow this. Attenuation is the removal of photons from a beam of X- or gamma rays as it passes through matter. Attenuation is caused by both absorption and scattering of the primary photons. At low photon energies

(<26 keV), the photoelectric effect dominates the attenuation processes in soft tissue. When higher energy photons interact with low Z materials (e.g., soft tissue), Compton scattering dominates (Fig).

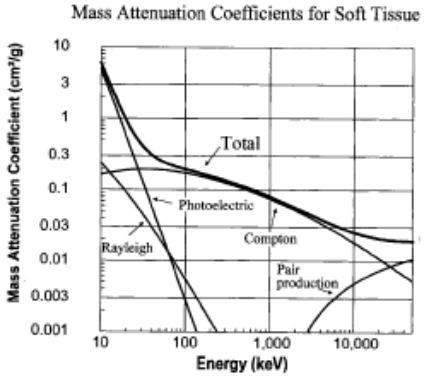


**Figure 1.9:** *Graph of the Rayleigh, photoelectric, Compton, pair production, and total mass attenuation coefficients for soft tissue (Z = 7) as a function of energy.*

Rayleigh scattering occurs in medical imaging with low probability, comprising about 10% of the interactions in mammography and 5% in chest radiography.

### 1.4.1 Linear attenuation coefficient

The fraction of photons removed from a mono energetic beam of X- or gamma rays per unit thickness of material is called the linear attenuation coefficient ($\mu$), typically expressed in $cm^{-1}$. The number of photons removed from the beam traversing a very small thickness $\Delta x$ can be expressed as:

$$n = \mu \cdot N \cdot \Delta x \tag{1.4}$$

where n = the number of photons removed from the beam, and N = the number of photons incident on the material. The attenuation process is continuous from the front surface of the attenuating material to the back exiting surface. To accurately calculate the number of photons removed from the beam using Equation 3-5, multiple calculations utilizing very small thicknesses of material ($\Delta x$) would be required. For a monoenergetic beam of photons incident upon either thick or thin slabs of material, an exponential relationship exists between the number of incident photons ($N_0$) and those that are transmitted ($N$) through a thickness $x$ without interaction:

$$N = N_0 \cdot e^{-\mu x} \tag{1.5}$$

The linear attenuation coefficient is the sum of the individual linear attenuation coefficients for each type of interaction:

$$\mu = \mu_{Rayleigh} + \mu_{photoelectriceffect} + \mu_{Comptonscatter} + \mu_{pairproduction} \tag{1.6}$$

In the diagnostic energy range, the linear attenuation coefficient decreases with increasing energy except at absorption edges (e.g., K-edge). The linear attenuation coefficient for soft tissue ranges from ~40.35 to ~0.16 $cm^{-1}$ for photon energies ranging from 30 to 100 keV.

### 1.4.2 Mass attenuation coefficient

For a given thickness, the probability of interaction is dependent on the number of atoms per volume. This dependency can be overcome by normalizing the linear attenuation coefficient for the density of the material. The linear attenuation coefficient, normalized to unit density, is called the mass attenuation coefficient:

$$Mass Attenuation Coefficient(\mu/\rho)[cm^2/g] = \frac{Linear Attenuation Coefficient(\mu)[cm^{-1}]}{Density of Material(\rho)[g/cm^3]} \quad (1.7)$$

The mass attenuation coefficient is independent of density. However, in radiology, we do not usually compare equal masses. Instead, we usually compare regions of an image that correspond to irradiation of adjacent volumes of tissue. Therefore, density, the mass contained within a given volume, plays an important role.

### 1.4.3 Half value layer

The half value layer (HVL) is defined as the thickness of material required to reduce the intensity of an X- or gamma-ray beam to one-half of its initial value. The HVL of a beam is an indirect measure of the photon energies (also referred to as the quality) of a beam, when measured under conditions of "good" or narrow-beam geometry. Narrow-beam geometry refers to an experimental configuration that is designed to exclude scattered photons from being measured by the detector. In broad-beam geometry, the beam is sufficiently wide that a substantial fraction of scattered photons remain in the beam. These scattered photons reaching the detector (Fig) result in an underestimation of the attenuation (i.e., an overestimated HVL). X-ray beams in radiology are typically composed of a spectrum of energies, dubbed a polyenergetic beam. The determination of the HVL in diagnostic radiology is a way of characterizing the hardness of the X-ray beam. The HVL, usually measured in millimetres of aluminium (mm AI) in diagnostic radiology, can be converted to a quantity called the effective energy. The effective energy of a polyenergetic X-ray beam is essentially an estimate of the penetration power of the X-ray beam, as if it were a monoenergetic beam.

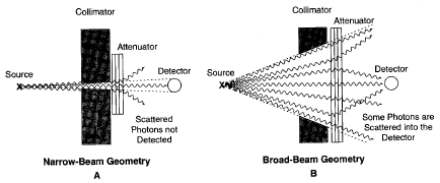


**Figure 1.10:** *A: Narrow-beam geometry means that the relationship between the source shield and detector are such that only non-attenuated photons interact with the detector. B: In broadbeam geometry attenuated photons may be scattered into the detector; thus the apparent attenuation is lower compared with narrow-beam conditions.*

One cannot predict the range of a single photon in matter. In fact, the range can vary from zero to infinity. However, the average distance traveled before interaction can be calculated from the linear attenuation coefficient or the HVL of the beam. This length, called the mean free path (MFP) of the photon beam, is

$$MFP = \frac{1}{\mu} = \frac{1}{0.693/HVL} = 1.44HVL \tag{1.8}$$

The lower energy photons of the polyenergetic X-ray beam will preferentially be removed from the beam while passing through matter. The shift of the X-ray spectrum to higher effective energies as the beam transverses matter is called beam hardening (Fig. 3-16). Low-energy (soft) X-rays will not penetrate most tissues in the body; thus their removal reduces patient exposure without affecting the diagnostic quality of the exam. X-ray machines remove most of this soft radiation with filters, thin plates of aluminum, or other materials placed in the beam. This filtering will result in an X-ray beam with a higher effective energy, and thus a larger HVL. The homogeneity coefficient is the ratio of the first to the second HVL and describes the polyenergetic character of the beam. A monoenergetic source of gamma rays has a homogeneity coefficient equal to 1. The effective (average) energy of an X-ray beam from a typical diagnostic X-ray tube is one-third to one-half the maximal value and gives rise to an "effective $\mu$" - the attenuation coefficient that would be measured if the X-ray beam were monoenergetic at that "effective" energy.

# Chapter 2

# X-rays Production and X-ray Tube

X-rays are produced when highly energetic electrons interact with matter and convert their kinetic energy into electromagnetic radiation. A device that accomplishes such a task consists of an electron source, an evacuated path for electron acceleration, a target electrode, and an external energy source to accelerate the electrons. Specifically, the X-ray tube insert contains the electron source and target within an evacuated glass or metal envelope; the tube housing provides shielding and a coolant oil bath for the tube insert; collimators define the X-ray field; and the generator is the energy source that supplies the voltage to accelerate the electrons. The generator also permits control of the X-ray output through the selection of voltage, current, and exposure time. These components work in concert to create a beam of X-ray photons of well-defined intensity, penetrability, and spatial distribution. In this chapter, the important aspects of the X-ray creation process, characteristics of the X-ray beam, and details of the equipment are discussed.

## 2.1 Production of X-rays

A simplified diagram of an X-ray tube (Fig. 5-1) illustrates the minimum components. A large voltage is applied between two electrodes (the cathode and the anode) in an evacuated envelope. The cathode is negatively charged and is the source of electrons; the anode is positively charged and is the target of electrons. As electrons from the cathode travel to the anode, they are accelerated by the electrical potential difference between these electrodes and attain kinetic energy. The electric potential difference, also called the voltage, is defined in Appendix A and the SI unit for electric potential difference is the volt (Y). The kinetic energy gained by an electron is proportional to the potential difference between the cathode and the anode.

On impact with the target, the kinetic energy of the electrons is converted to other forms of energy. The vast majority of interactions produce unwanted heat by small collisional energy exchanges with electrons in the target. This intense heating limits the number of X-ray photons that can be produced in a given time without destroying the target. Occasionally (about 0.5% of the time), an electron comes within the proximity of a positively charged nucleus in the target electrode. Coulombic forces attract and decelerate the electron, causing a significant loss of kinetic energy and a change in

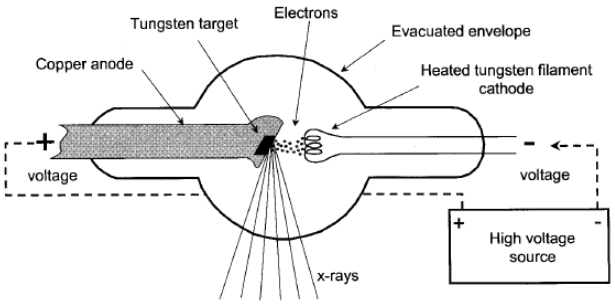


**Figure 2.1:** *Minimum requirements for X-ray production include a source and target of electrons, an evacuated envelope, and connection of the electrodes to a high-voltage source.*

the electron's trajectory. An X-ray photon with energy equal to the kinetic energy lost by the electron is produced (conservation of energy). This radiation is termed bremsstrahlung, a German word meaning "braking radiation." The probability of an electron's directly impacting a nucleus is extremely low, simply because, at the atomic scale, the atom comprises mainly empty "space" and the nuclear cross-section is very small. Therefore, lower X-ray energies are generated in greater abundance, and the number of higher-energy X-rays decreases approximately linearly with energy up to the maximum energy of the incident electrons. A bremsstrahlung spectrum depicts the distribution of X-ray photons as a function of energy. The unfiltered bremsstrahlung spectrum (Fig) shows a ramp-shaped relationship between the number and the energy of the X-rays produced, with the highest X-ray energy determined by the peak voltage (kVp) applied across the X-ray tube. Filtration refers to the removal of X-rays as the beam passes through a layer of material. A typical filtered bremsstrahlung spectrum (see Fig) shows a distribution with no X-rays below about 10 keY: With filtration, the lower-energy X-rays are preferentially absorbed, and the average X-ray energy is typically about one third to one half of the highest X-ray energy in the spectrum.

Major factors that affect X-ray production efficiency include the atomic number of the target material and the kinetic energy of the incident electrons (which is determined by the accelerating potential difference).
One part of radiation in the spectrum in the less important amount compared to the bremsstrahlung radiation , but nonetheless significant, are the characteristics radiations. Characteristic X-rays are produced when an element is bombarded with high-energy electrons. When a high-energy electron (the incident electron) strikes a bound electron (the target electron) in an atom, the target electron is ejected from the inner shell of the atom. After the electron has been ejected, the atom is left with a vacant energy level, also known as a core hole. Outer-shell electrons then fall into the inner shell, emitting quantized photons with an energy level equivalent to the energy difference between the higher and lower states. Each element has a unique set of energy levels, and thus the transition from higher to lower energy levels produces X-rays with frequencies that are characteristic to each element. When an electron falls from the L shell to the K shell, the X-ray emitted is called a K-alpha X-ray. Similarly, when an electron falls from the M shell to the K shell, the X-ray emitted is called a K-beta X-ray.

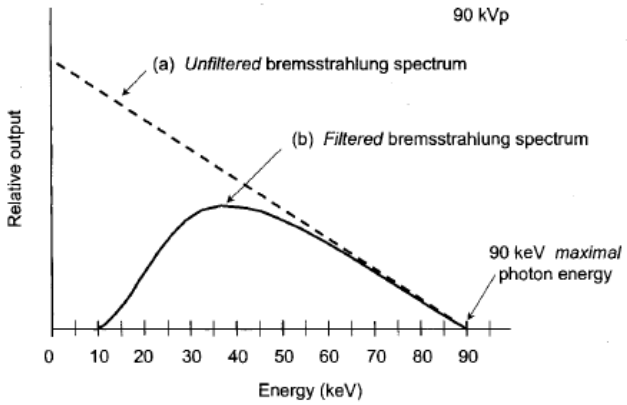


**Figure 2.2:** *The bremsstrahlung energy distribution for a 90 kVp acceleration potential. (a) The unfiltered bremsstrahlung spectrum (dashed line) shows a greater probability of low-energy X-ray photon production that is inversely linear with energy up to the maximum energy of 90 keY. (b) The filtered spectrum shows the preferential attenuation of the lowest-energy X-ray photons.*

## 2.2 X-ray Tubes

The X-ray tube provides an environment for X-ray production via bremsstrahlung and characteristic radiation mechanisms. Major components are the cathode, anode, rotor/stator, glass (or metal) envelope, and tube housing.

### 2.2.1 Cathode

The source of electrons in the X-ray tube is the cathode, which is a helical filament of tungsten wire surrounded by a focusing cup (Fig. 2.5). This structure is electrically connected to the filament circuit. Electrical resistance heats the filament and releases electrons via a process called thermionic emission. The electrons liberated from the filament flow through the vacuum of the X-ray tube when a positive voltage is placed on the anode with respect to the cathode. Adjustments in the filament current (and thus in the filament temperature) control the tube current. A trace of thorium in the tungsten filament increases the efficiency of electron emission and prolongs filament life. The focusing cup, also called the cathode block, surrounds the filament and shapes the electron beam width. The voltage applied to the cathode block is typically the same as that applied to the filament. This shapes the lines of electrical potential to focus the electron beam to produce a small interaction area (focal spot) on the anode.

The width of the focusing cup slot determines the focal spot width, the filament length determines the focal spot length. X-ray tubes for diagnostic imaging typically have two filaments of different lengths, each in a slot machined into the focusing cup. Selection of one or the other filament determines the area of the electron distribution (small or large focal spot) on the target. The filament current determines the filament temperature and thus the rate of thermionic electron emission. As the electrical resistance to the filament current heats the filament, electrons are emitted from its surface. When no voltage is applied between the anode and the cathode of the X-ray tube, an electron cloud, also called a space charge cloud, builds around the filament. Applying a positive high voltage to the anode with respect to the cathode accelerates

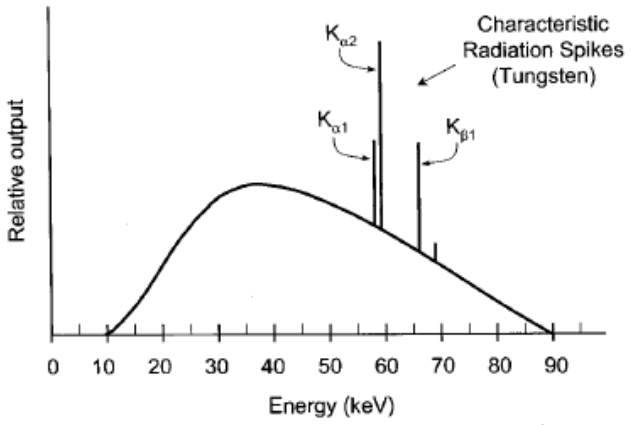


**Figure 2.3:** *The filtered spectrum of bremsstrahlung and characteristic radiation from a tungsten target with a potential difference of 90 kVp illustrates specific characteristic radiation energies from $K_\alpha$ and $K_\beta$ transitions.*

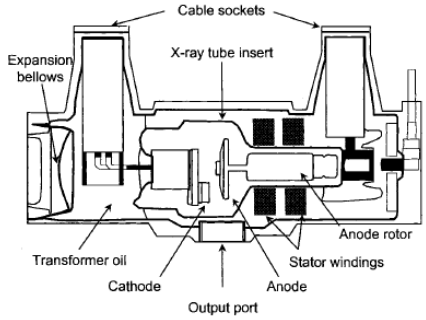


**Figure 2.4:** *The major components of a modern X-ray tube and housing assembly.*

the electrons toward the anode and produces a tube current. Small changes in the filament current can produce relatively large changes in the tube current.

### 2.2.2 Anode

The anode is a metal target electrode that is maintained at a positive potential difference relative to the cathode. Electrons striking the anode deposit the most of their energy as heat, with a small fraction emitted as X-rays. Consequently, the production of X-rays, in quantities necessary for acceptable image quality, generates a large amount of heat in the anode. To avoid heat damage to the X-ray tube, the rate of X-ray production must be limited. Tungsten (W, Z = 74) is the most widely used anode material because of its high melting point and high atomic number. A tungsten anode can handle substantial heat deposition without cracking or pitting of its surface. An alloy of 10% rhenium and 90% tungsten provides added resistance to surface damage. Molybdenum (Mo, Z = 42) and rhodium (Rh, Z = 45) are used as anode materials in mammographic X-ray tubes. These materials provide useful characteristic X-rays for breast imaging. X-ray tubes have stationary and rotating anode configurations. Despite their increased complexity in design and engineering,

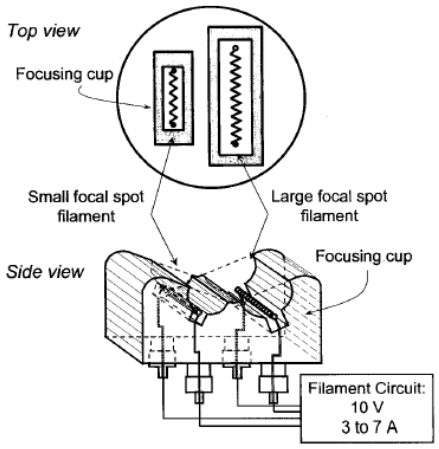


**Figure 2.5:** *The X-ray tube cathode structure consists of the filament and the focusing (or cathode) cup. Current from the filament circuit heats the filament, which releases electrons by thermionic emission.*

rotating anodes are used for most diagnostic X-ray applications, mainly because of their greater heat loading and consequent higher X-ray output capabilities. Electrons impart their energy on a continuously rotating target, spreading thermal energy over a large area and mass of the anode disk (Fig. 2.6)

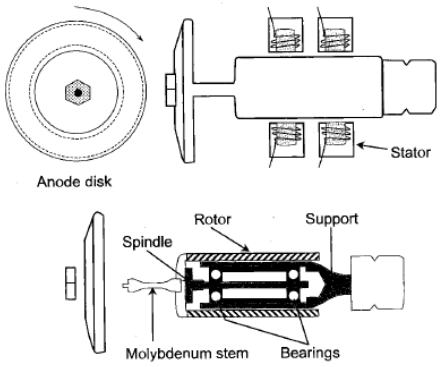


**Figure 2.6:** *The anode of a rotating anode X-ray tube comprises a tungsten disk mounted on a bearingsupported rotor assembly (front view, top left; side view, top right). The rotor consists of a copper and iron laminated core and forms part of an induction motor. A molybdenum stem (molybdenum is a poor heat conductor) connects the rotor to the anode to reduce heat transfer to the rotor bearings (bottom).*

A bearing-mounted rotor assembly supports the anode disk within the evacuated X-ray tube insert. The rotor consists of copper bars arranged around a cylindrical iron core. A series of electromagnets surrounding the rotor outside the X-ray tube envelope makes up the stator, and the combination is known as an induction motor. X-ray machines are designed so that the X-ray tube will not be energized if the anode is not up to full speed; this is the cause for the short delay (1 to 2 seconds) when the X-ray tube exposure button is pushed.

### 2.2.3 Anode angle and focal spot size

The anode angle is defined as the angle of the target surface with respect to the central ray in the X-ray field (Fig. 2.7). Anode angles in diagnostic X-ray tubes, other than some mammography tubes, range from 7 to 20 degrees. Focal spot size is defined in two ways. The actual focal spot size is the area on the anode that is struck by electrons, and it is primarily determined by the length of the cathode filament and the width of the focusing cup slot. The effective focal spot size is the length and width of the focal spot as projected down the central ray in the X-ray field. The effective focal spot width is equal to the actual focal spot width and therefore is not affected by the anode angle. However, the anode angle causes the effective focal spot length to be smaller than the actual focal spot length. The effective and actual focal spot lengths are related as follows:

$$\text{Effective focal length} = \text{Actual focal length X sin } \Theta$$

where $\Theta$ is the anode angle. This foreshortening of the focal spot length, as viewed down the central ray, is called the line focus principle.

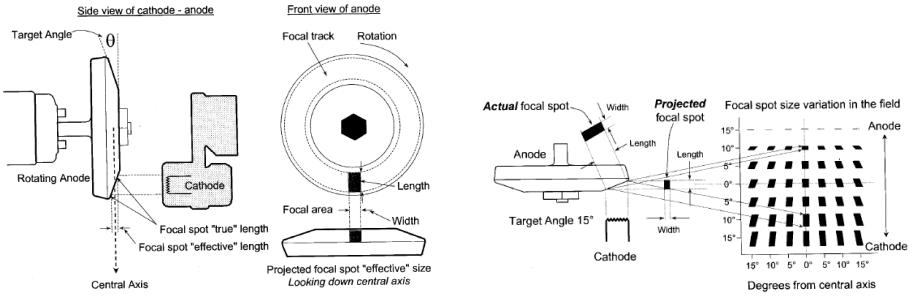


**(a)** *The anode (target) angle, Θ, is defined as the angle of the target surface in relation to the central ray. The focal spot length, as projected down the central axis, is foreshortened, according to the line focus principle (lower right).*

**(b)** *Variation of the effective focal spot size in the image field occurs along the anode-cathode direction. Focal spot distributions are plotted as a function of projection angle in degrees from the central axis, the parallel (vertical axis), and the perpendicular (horizontal axis).*

**Figure 2.7:** Anode angle and his variation.

The effective focal spot length varies with the position in the image plane, in the anode-cathode (A-C) direction. Toward the anode side of the field the projected length of the focal spot shortens, whereas it lengthens towards the cathode side of the field (Fig. 2.7). In the width dimension, the focal spot size does not change appreciably with position in the image plane. The nominal focal spot size (width and length) is specified at the central ray of the beam.

### 2.2.4 Heel effect

The heel effect refers to a reduction in the X-ray beam intensity toward the anode side of the X-ray field (Fig. 2.8). X-rays are produced isotropically at depth in the anode structure. Photons directed toward the anode side of the field transit a greater thickness of the anode and therefore experience more attenuation than those directed toward the cathode side of the field. For a given field size, the heel effect is less prominent with a longer source-to-image distance (SID), because the image receptor

subtends a smaller beam angle. The X-ray tube is best positioned with the cathode over thicker parts of the patient and the anode over the thinner parts, to better balance the transmitted X-ray photons incident on the image receptor.

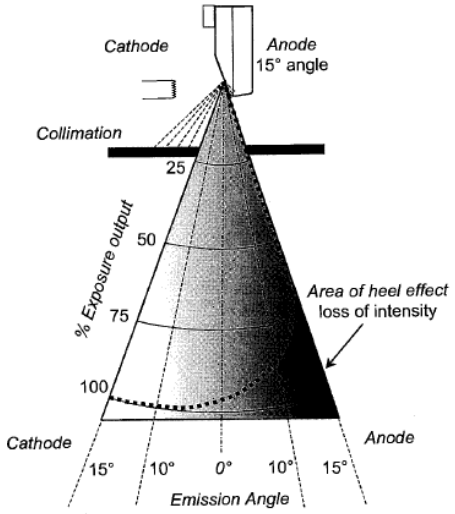


**Figure 2.8:** *The heel effect is a loss of intensity on the anode side of the X-ray field of view. It is caused by attenuation of the X-ray beam by the anode.*

### 2.2.5 Off-focus radiation

Off-focus radiation results from electrons in the X-ray tube that strike the anode outside the focal spot area. A small fraction of electrons scatter from the target and are accelerated back to the anode outside the focal spot. These electrons create a low intensity X-ray source over the face of the anode. Off-focus radiation increases patient exposure, geometric blurring, and background fog. A small lead collimator placed near the X-ray tube output port can reduce off-focus radiation by intercepting X-rays that are produced at a large distance from the focal spot. X-ray tubes that have a metal enclosure with the anode at the same electrical potential (i.e., grounded anode) reduce off-focus radiation because stray electrons are just as likely to be attracted to the metal envelope as to the anode.

## 2.3 Factors affecting X-ray emission

The output of an X-ray tube is often described by the terms quality, quantity, and exposure. Quality describes the penetrability of an X-ray beam, with higher energy X-ray photons having a larger HVL and higher "quality." Quantity refers to the number of photons comprising the beam. Exposure, defined in Chapter 3, is nearly proportional to the energy fluence of the X-ray beam and therefore has quality and quantity associated characteristics. X-ray production efficiency, exposure, quality, and quantity are determined by six major factors: X-ray tube target material, voltage, current, exposure time, beam filtration, and generator waveform.

1. The target (anode) material affects the efficiency of bremsstrahlung radiation production, with output exposure roughly proportional to atomic number. Incident electrons are more likely to have radiative interactions in higher-Z materials. The energies of characteristic X-rays produced in the target depend on the target material. Therefore, the target material affects the quantity of bremsstrahlung photons and the quality of the characteristic radiation.

2. Tube voltage (kVp) determines the maximum energy in the bremsstrahlung spectrum and affects the quality of the output spectrum. In addition, the efficiency of X-ray production is directly related to tube voltage. Exposure is approximately proportional to the square of the kVp in the diagnostic energy range:
$$Exposure \propto kVp^2 \tag{2.1}$$
An increase in k Vp increases the efficiency of X-ray production and the quantity and quality of the X-ray beam. Changes in the kVp must be compensated by corresponding changes in mAs to maintain the same exposure.

3. The tube current (mA) is equal to the number of electrons flowing from the cathode to the anode per unit time. The exposure of the beam for a given kVp and filtration is proportional to the tube current.

4. The exposure time is the duration of X-ray production. The quantity of X-rays is directly proportional to the product of tube current and exposure time (mAs).

5. The beam filtration modifies the quantity and quality of the X-ray beam by selectively removing the low-energy photons in the spectrum. This reduces the photon number (quantity) and shifts the average energy to higher values, increasing the quality.

6. The generator waveform affects the quality of the emitted X-ray spectrum. For the same kVp, a single-phase generator provides a lower average potential difference than does a three-phase or high-frequency generator. Both the quality and quantity of the X-ray spectrum are affected.

In summary, the X-ray quantity is approximately proportional to $Z_{target} \cdot kVp2 \cdot mAs$. The X-ray quality depends on the kVp, the generator waveform, and the tube filtration. Exposure depends on both the quantity and quality of the X-ray beam. Compensation for changes in kVp with radiographic techniques requires adjustments of mAs on the order of the fifth power of the kVp ratio, because kVp determines quantity, quality, and transmission through the object, whereas mAs determines quantity only.

### 2.3.1 Roughness

X-ray spectra produced with x-ray tubes depend primarily on tube voltage and voltage ripple, and the attenuation of the photons within the x-ray tube and the tube housing. In diagnostic units some minimum photon attenuation by the absorbing materials between the anode and beam exit is mandatory to reduce radiation dose to the patient from the low energy X-rays in the spectrum. Some additional filters are introduced to achieve a filtration of an equivalent in aluminium of typically 2.5 mm. In therapy and metrology various filter combinations are used to achieve the radiation qualities required. Besides, the attenuation of the X-rays in the anode material itself also contributes to filtration. The X-rays produced by electrons slowed down in the

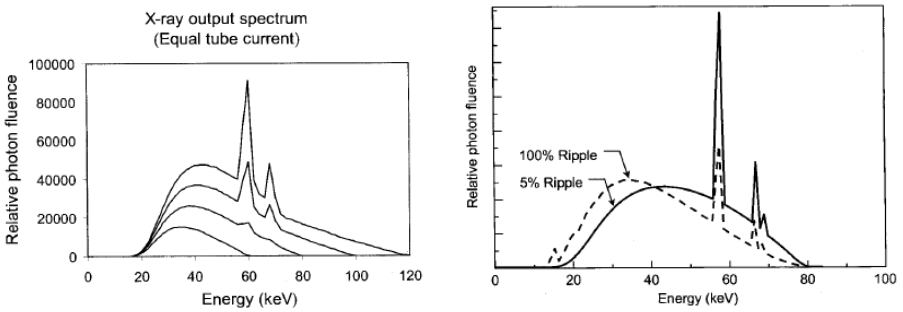


**(a)** *X-ray tube output intensity varies strongly with tube voltage (kVp). In this example, the same tube current and exposure times (mAs) are compared for 60 to 120 kVp. The relative area under each spectrum roughly follows a squared dependence (characteristic radiation is ignored).*

**(b)** *Output intensity (bremsstrahlung) spectra for the same tube voltage (kVp) and the same tube current and exposure time (mAs) demonstrate the higher effective energy and greater output of a threephase or high-frequency generator voltage waveform (approximately 5% voltage ripple), compared with a single-phase generator waveform (100% voltage ripple).*

**Figure 2.9:** Factors affecting X-ray emission.

anode encounter some attenuation in the anode material depending on the anode angle and the beam direction. Hence, an effective inherent filtration includes both attenuation in the anode and in all other tube materials. The condition of the anode surface and the deposition of sputtered tungsten on the tube envelope have also been made responsible for an increased effective inherent filtration [4]. Tungsten deposits on the inner side of the tube are found to be much less than 1 $\mu$m in thickness [9] [12] and consequently should give little contribution to attenuation. Less data are available on the influence of anode roughness on spectra and spectral parameters [9].

# Chapter 3

# CT and Spectral CT

In conventional radiography, subtle differences of less than about 5 percent in subject contrast (i.e., x-ray attenuation in the body) are not visible in the image. This limitation exists for the following reasons [7] [13] :

1. The projection of three-dimensional anatomic information onto a two dimensional image receptor obscures subtle differences in x-ray transmission through structures aligned parallel to the x-ray beam. Although conventional tomography resolves this problem to some degree, structures above and below the tomographic section may remain visible as "ghosts" in the image if they differ significantly in their x-ray attenuating properties from structures in the section.

2. Conventional image receptors (i.e., film) are not able to resolve small differences (e.g., 2%) in the intensity of incident radiation.

3. Large-area x-ray beams used in conventional radiography produce considerable scattered radiation that interferes with the display of subtle differences in subject contrast.

To a significant degree, each of these difficulties is eliminated in computed tomography (CT). Hence, differences of a few tenths of a percent in subject contrast are revealed in the CT image. Although the spatial resolution of a millimeter or so provided by CT is notably poorer than that provided by conventional radiography, the superior visualization of subject contrast, together with the display of anatomy across planes (e.g., cross-sectional) that are not accessible by conventional imaging techniques, make CT exceptionally useful for visualizing anatomy in many regions of the body.

## 3.1 Principle of Computed Tomographic Imaging

In early CT imaging devices ("scanners") a narrow x-ray beam is scanned across a patient in synchrony with a radiation detector on the opposite side of the patient. If the beam is monoenergetic or nearly so, the transmission of x rays through the patient is

$$I = I_0 \cdot e^{-\mu x} \tag{3.1}$$

In this equation the patient is assumed to be a homogeneous medium. If the x-ray beam is intercepted by two regions with attenuation coefficients $\mu 1$ and $\mu 2$ and thicknesses $x1$ and $x2$, the x-ray transmission is

$$I = I_0 \cdot e^{-(\mu_1 x_1 + \mu_2 x_2)} \tag{3.2}$$

If many (n) regions with different linear attenuation coefficients occur along the path of x-rays, the transmission is

$$I = I_0 \cdot e^{-\sum_{i=1}^{n} \mu_i x_i} \tag{3.3}$$

where $-\sum_{i=1}^{n} \mu_i x_i = \mu_1 x_1 + \mu_2 x_2 + \cdots + \mu_n x_n$ and the fractional transmission $I/I_0$ is

$$e^{-\sum_{i=1}^{n} \mu_i x_i} \tag{3.4}$$

With a single transmission measurement, the separate attenuation coefficients cannot be determined because there are too many unknown values of $\mu_i$ in the equation. However, with multiple transmission measurements in the same plane but at different orientations of the x-ray source and detector, the coefficients can be separated so that a cross-sectional display of attenuation coefficients is obtained across the plane of transmission measurements. By assigning gray levels to different ranges of attenuation coefficients, a gray-scale image can be produced that represents various structures in the patient with different x-ray attenuation characteristics. This gray-scale display of attenuation coefficients constitutes a CT image. In early (first-generation) CT scanners, multiple x-ray transmission measurements are obtained by scanning a pencil-like beam of x-rays and an NaI detector in a straight line on opposite sides of the patient (Fig).

During this translational scan of perhaps 40 cm in length, multiple (e.g., 160) measurements of x-ray transmission are obtained. Next, the angular orientation of the scanning device is incremented 1 degree, and a second translational scan of 160 transmission measurements is performed. This process of translational scanning separated by 1-degree increments is repeated through an arc of 180 degrees. In this manner, 160·180 = 28,800 x-ray transmission measurements are accumulated. These measurements are transmitted to a computer equipped with a mathematical package for reconstructing an image of attenuation coefficients across the anatomic plane defined by the scanning x-ray beam.

### 3.1.1 Artifact in Computed Tomography

#### Beam Hardening

Like all medical x-ray beams, CT uses a polyenergetic x-ray spectrum, with energies ranging from about 25 to 120 keV: Furthermore, x-ray attenuation coefficients are energy dependent: after passing through a given thickness of patient, lower-energy x-rays are attenuated to a greater extent than higher-energy x-rays are. Therefore, as the x-ray beam propagates through a thickness of tissue and bone, the shape of the spectrum becomes skewed toward the higher energies. Consequently, the average energy of the x-ray beam becomes greater ("harder") as it passes through tissue. Because the attenuation of bone is greater than that of soft tissue, bone causes more beam hardening than an equivalent thickness of soft tissue. The beam-hardening phenomenon induces artifacts in CT because rays from some projection angles are hardened to a differing extent than rays from other angles, and this confuses the reconstruction algorithm.

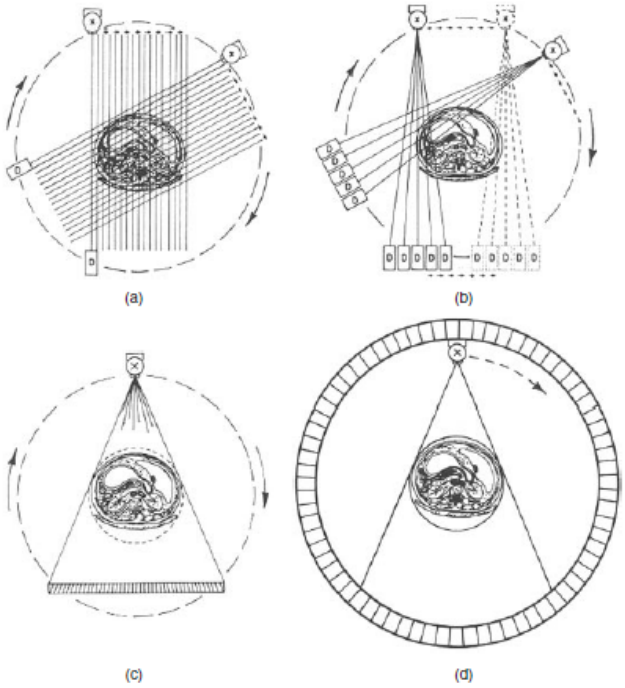


**Figure 3.1:** *Scan motions in computed tomography.* ***A****: first-generation scanner using a pencil x-ray beam and a combination of translational and rotational motion.* ***B****: Second-generation scanner with a fan x-ray beam, multiple detectors, and a combination of translational and rotational motion.* ***C****: Third-generation scanner using a fan x-ray beam and smooth rotational motion of x-ray tube and detector array.* ***D****: Fourth-generation scanner with rotational motion of the x-ray tube within a stationary circular array of 600 or more detectors.*

Most CT scanners include a simple beam-hardening correction algorithm that corrects for beam hardening based on the relative attenuation of each ray, and this helps to some extent. More sophisticated two-pass beam-hardening correction algorithms have been implemented by some manufacturers, and these correction techniques can substantially reduce artifacts resulting from beam hardening.

### Motion artifacts

Motion artifacts occur when the patient moves during the acquisition. Small motions cause image blurring, and larger physical displacements during CT image acquisition produce artifacts that appear as double images or image ghosting. If motion is suspected in a CT image, the adjacent CT scans in the study may be evaluated to distinguish fact from artifact. In some cases, the patient needs to be rescanned.

### Partial volume averaging

The CT number in each pixel is proportional to the average $\mu$ in the corresponding voxel. Some voxels in the image, however, contain a mixture of different tissue types. When this occurs, for example with bone and soft tissue, the $\mu$ is not representative of either tissue but instead is a weighted average of the two different $\mu$ values. Partial

volume averaging is most pronounced for softly rounded structures that are almost parallel to the CT slice. The most evident example is near the top of the head, where the cranium shares a substantial number of voxels with brain tissue, causing details of the brain parenchyma to be lost because the large $\mu$ of bone dominates. This situation is easily recognizable and therefore seldom leads to misdiagnosis. Partial volume artifacts can lead to misdiagnosis when the presence of adjacent anatomic structures is not suspected. This last problem described could be solved or at least receive a greatly improvement thanks to the development of a new technique that will be described in the next paragraph.

## 3.2 Spectral CT and his advantages

Recent years have seen increased research efforts in energy-sensitive, photon counting detectors [11] and their application to computed tomography imaging [20]. As today's commercially available computed tomography scanners exclusively employ scintillation detectors operated in current-integrating mode, a part of the information about the attenuation by the object carried by the transmitted flux of x-rays is lost during the detection process. Hence, it is reasonable to ask to what extent the additional information acquired with the help of more advanced detection technology can be used to the benefit of a better clinical diagnosis, the reduction of the dose administered to the patient or to the development of novel CT imaging applications. Intuitively it is clear that the optimal data acquisition in CT would consist of a precise measurement of the energies of all individual x-ray photons in the transmitted x-ray spectrum, thus operating each detector pixel in spectroscopic mode. In practice, however, it turns out that near-optimal imaging performance can be obtained with much less sophisticated detection techniques [2], because the relative contributions to the total x-ray attenuation caused by the photo-electric effect and the Compton effect do not vary strongly for different types of human tissue. For the case of basis material decompositions it has been shown recently that all the information contained in the transmitted spectrum regarding a given N-dimensional basis material decomposition of the object can be retrieved by performing a number of N appropriately weighted spectral measurements. However, the experimental realization of these remains challenging [5].

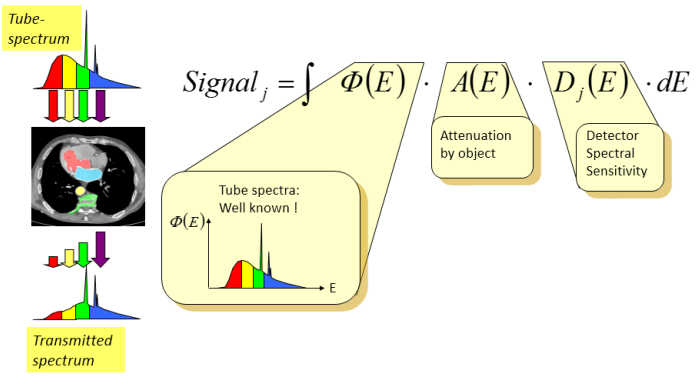


**Figure 3.2:** *Illustration of the principles that underpin the spectral CT, what is measured and what is necessary to know.*

It has been further shown that the number of energy thresholds required to acquire

most of the available, additional information by energy-discriminating photon-counting detectors is rather small: about 4-6 if the energy thresholds are optimized for the imaging task. A new kind of application is *spectral K-edge imaging technique*[24]. In this technique, a contrast medium is administered having, as is usual for CT, an element with high atomic number as its active component. The energy of the attenuation K-edge is characteristic for the element. By adjusting one of the energy thresholds in the detector to the K-edge of the contrast element, the technique allows to distinguish between the attenuation caused by the contrast medium and the surrounding non-contrasted tissue. Thus, a physical mechanism is provided that allows the selective imaging of the material being administered. The decomposition of the attenuation can be achieved, e.g., with the help of the maximum likelihood method. In the situation in which two different contrast media (based on two different elements and, thus, different K-edge energies) are present at the same time. Then, a first of two available energy thresholds is adjusted to the K-edge energy of the first element and a second available energy threshold to the K-edge energy of the second element. Hence, it becomes possible to separate between the attenuation coming from the first contrast agent, the second contrast agent and the surrounding tissue. Note that in the latter case of two contrast agents, at least four energy thresholds are required as the correct modelling of human tissue requires two basis materials.

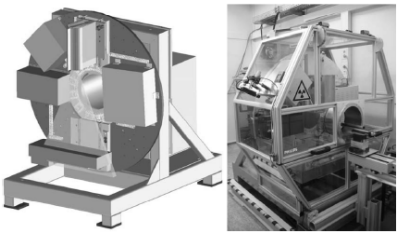

**Figure 3.3:** *Schematic drawing and photograph of the pre-clinical spectral CT. The key components on a rotating gantry are a micro-focus x-ray tube (top) and a single-line energy-binning photon-counting detector (bottom).*

On these principles described above major companies have started developing systems to commercialize this new type of CT, called spectral CT. The two approaches used are quite different but are based on the same principle. The first and easiest idea is to change the voltage, using low and high kV and the same detector; how is it possible do that? Siemens has implemented the use of two detectors and two tubes at the same time. In this way you have two different spectra at the same time, and it's like having two different measurement systems. The approach used by Philips instead, is a double decade detector means having two photodiodes in a single pixels, but two separate levels of scintillators. In this way there is a vertical photodiode with the two separated level. So this meaning that is it possibile to measure low energy range for the upper part of the photodiode and high energy layer for the lower. If the two results are combined, the final result is the same of the actual single scintillator. Of course the main problem is the increasing of the noise and the decreasing of the SNR; but in this way is it possible to measure on parallel and reduce the patient dose as well. Just one tube and both of informations. Difference between Siemens, is that in the Siemens approach the tube is not fixed and it needs a rotation of 90 degree and for that reason

the process will not be fast enough for some application. At least now, both company agree that the final technology will be the photon counting technology and both works on that direction. The benefits are mainly same time and definitely a better energy resolution.

# Chapter 4

# Simulation software

A detailed review on X-ray spectra simulation can be found e.g. in [6] from which a summary is given in this section. The intensity of the X-ray continuum at a given photon energy has been computed by many authors concerned with electron probe micro-analysis [22] [23]. The results are normally compared to the theory developed by Kramers [17]. However, very few authors have computed X-ray spectra and compared them to high resolution, constant potential spectra with accurately known inherent filtration. Unsworth and Greening (1970) modified Kramers' theory (to allow for absorption in the target) and generated spectra up to 50 kV, but only compared the total energy emission for spectra up to 30 kV with experimental data. Sundararaman, Prasad and Vora (1973) used a Monte Carlo method to generate spectra and compared their results with Kramers' theory and the experimental spectra of Epp and Weiss [10] measured with a NaI detector.

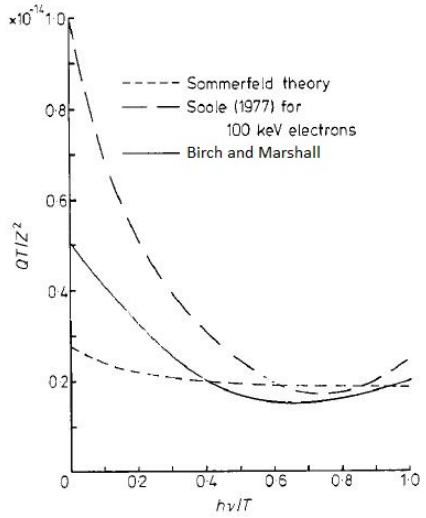


**Figure 4.1:** *Comparison of differential energy intensity Q with $h\nu/T$, where $h\nu$ is the photon energy and T is the electron energy (reproduced from [6]).*

The measured spectra were stated to have a voltage ripple of twenty-five per cent of the peak potential and the waveform was approximated mathematically for the

calculated spectra. Kramers [17] assumed that the original differential energy intensity was constant, and did not allow for the target absorption, the two parameters more or less masking each other as noted by Soole [26]. Soole [25] determined the varying differential energy intensity by matching data generated by Kramers' theory, modified to allow for target absorption, with attenuation measurements. However, Soole did not present spectra calculated using this theory, and on doing so we found that the target attenuation was too great, indicated by too large a drop at the tungsten K-edge at higher voltages when compared to measured spectra. If the target absorption was reduced by using more realistic values for the Thomson-Whiddington constant the spectra were found to be too soft. Sommerfeld (1931) produced a non-relativistic theory, which referred to ideally thin targets, for which Kirkpatrick and Wiedmann (1945) developed empirical equations to fit the values of the differential energy intensity. The variation with $hv$/T (where E = $hv$ is the photon energy and T is the electron energy) was considerably less than that suggested to Soole (see Fig 4.1) possibly due to the target absorption in the latter being too great. The purpose of Birch and Marshall work [6] was to develop a theory to give spectra that agreed with constant potential measured spectra for a range of voltages, filtrations and target angles.

## 4.1 Tucker Barnes Model (base of Philips simulation tools)

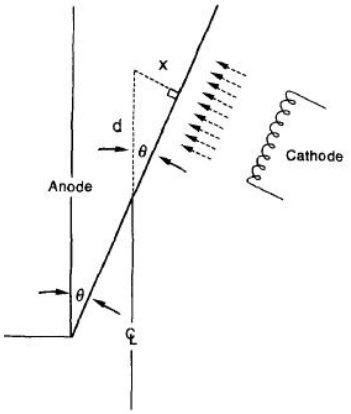


**Figure 4.2:** *X-ray tube geometry and the relation between depth of X-ray production (x) and X-ray photon path length through target (d). CL represent schematically the center line or central ray*

The semi-empirical model for generating tungsten target x-ray spectra, which the Philips simulation tools is based on, is the Tucker Barnes Model [27]. The model presented by these studies is more general then previous models in that characteristic and bremsstrahlung X-ray production is assumed to occur at different depths within the target. In addition, non-linear least-squares techniques were employed to obtain the best values for the model parameters. As a result good agreement is obtained over a wide range of X-ray tube potentials with the measured spectra utilized to fit the model parameters, both for shape and radiation exposure. The model allows one to compute spectra for different target angles. As shown in Fig 4.3 for 12.5° and 20°

targets, good agreement with measured spectra is obtained when this is done. Such is not the case with previously mentioned models (Kramers, Storm, and Birch and Marshall). Of interest is that by appropriately taking into account the difference in photon path length in the target and window, the model can also be employed to compute off-axis spectra.

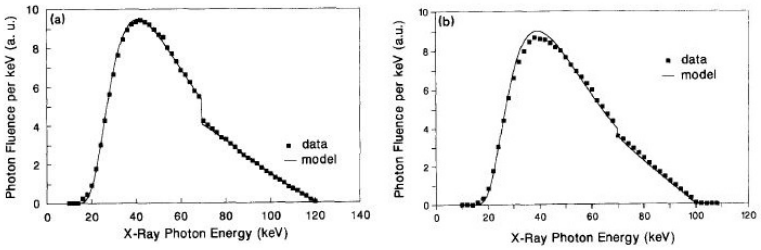


**Figure 4.3:** *Comparison of experimental and computed bremsstrahlung spectra for (a) Eimac* 12.5° *target X-ray tube at 120 kVcp and for (b) Machlett Aeromax* 20° *target X-ray tube at 100kVcp. In both cases spectra were normalized to the same area reproduced from [27].*

For all these listed reasons the Tucker Barnes model, is one of the most used for these kind of operations and is the model on that the Philips simulations software is based and it will be used in the following work.

# Chapter 5

# Set-up equipment

This chapter describes the main tools used for subsequent experiments and for the realization of the experimental set-up. The main components are the germanium detector, the X-ray tube, flat panel detector and the collimators.

## 5.1 Detector

[8] Semiconductor detectors are often used for the detection of charged particles and photons emitted by radioactive nuclei. Semiconductor detectors exhibit many desirable properties, including

1. a response that varies linearly with the energy deposited in the detector and is not influenced by the type of radiation that deposits the energy,
2. a negligible absorption of energy in the entrance window of the detector,
3. excellent energy resolution,
4. the formation of pulses with fast rise times,
5. small detector size.

The response mechanism of a semiconductor detector resembles that for an ionization chamber. Ionization produced within the sensitive volume of the detector is converted to a current pulse. Physically, the signals of drifting charges induce a current to the electrodes. The current pulse can be (or is de facto) converted into a voltage pulse after amplification and then it is counted. The size of the current pulse is proportional to the energy expended in the detector by the incident radiation. When compared with an ionization chamber, the current pulse is sharper and more accurately reflects the energy deposited on the detector. Also, the rise time of the pulse is shorter because the ionization is collected more rapidly. The CANBERRA Ultra-LEGe detector[1] (used in the experiment) has an energy reolution down to a few hundred (100-200) electron volts, providing resolution and increase the peak-to-background ratio.[8]. The Ultra-LEGe retains a high-energy efficiency intrinsic to germanium detectors because of moderate high atomic number (Z)[2], combined with a relatively high thickness (5-10 mm), and

[1] Ultra Low Energy Germanium Detectors (LEGe)
[2] Z=32, as compared to the semiconductor "reference" material Si with Z=14

thus the range of medical X-ray energies used in the experiments reasonable well. The graph below compares the efficiency of the high-energy side of the X-ray spectrum of a 5 mm thick germanium detector to typical silicon based detectors.

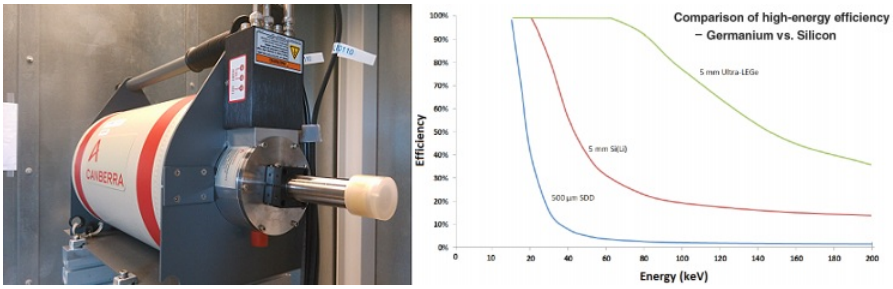


**Figure 5.1:** *Ultra LEGe detector and its skils*

A major advantage of the Ultra-LEGe detector structure is its low capacitance, which means that the detector maintains good energy resolution performance even at very short shaping times.

### 5.1.1 Pre-amplifier

Almost all radiation detectors exhibit low capacitance and high impedance. Signals from these detectors are distorted and severely attenuated if they are transmitted by a coaxial cable directly from the detector to an amplifier some distance away. To reduce these effects, a pre-amplifier may be inserted near the detector. The purpose of the pre-amplifier is to match the impedance of the detector with that of the amplifier. When this is done, the cable to the amplifier may be several feet long. Pre-amplifiers are used also to "clip" and "shape" the voltage pulse from the detector to meet the specifications of the amplifier. The standard type pre-amplifier used in our experiment on Ultra-LEGe detectors is the CANBERRA I-TRP model.

### 5.1.2 Pile-up

[28] Pulse pile-up happens when pulses arrives closer in time than the pulse resolution time for the system. Figure 5.2 shows an example of a $1^{st}$ order pulse pile-up where pulse 2 is riding on the tail of pulse 1.

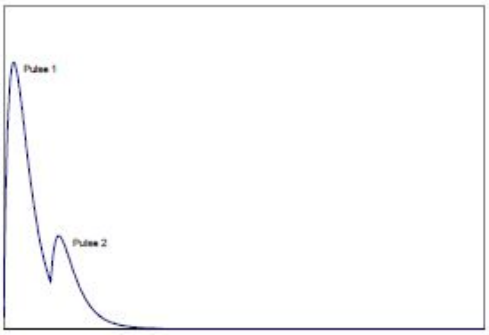


**Figure 5.2:** $1^{st}$ *order pulse pile-up where pulse 2 is riding on the tail of pulse 1.[28]*

When this occurs the system can't measure the pulse heights correctly. If the pulses are very close in time the system will simply record the two pulses as a single event with combined pulse amplitude (Pulse 1 + Pulse 2), this is also known as peak pile-up. If the pulses are spaced further apart the system may simply accept both events and record them with incorrect pulse amplitude, this is known as tail pile-up. In either case the events will end up in the wrong energy channels at higher energies and the spectrum will be contaminated leading to incorrect results when the spectra are further analyzed. The number of pile-up events depends strongly on the count rate of the system. At lower count rate $1^{st}$ order pile-up is dominant but as the count rate increases higher order pileup where 3 or more consecutive pulses are involved becomes significant. Figure 5.3 shows the effect 10% $1^{st}$ order peak pile-up has on a 137Cs spectrum. The clean spectrum has no recorded events above the photo peak at 662 keV whereas the pile-up spectrum has recorded events up to 2 x 662 keV.

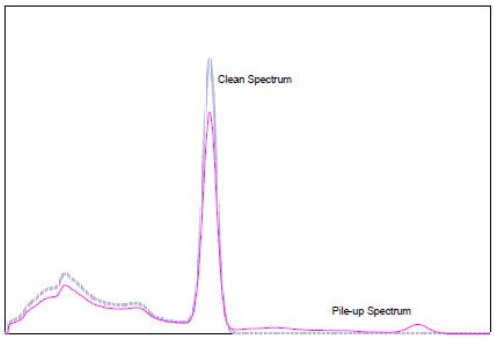


**Figure 5.3:** *The effect 10% $1^{st}$ order peak pile-up has on a 137Cs spectrum.[28]*

A good spectrometer will have build in pile-up rejection to minimize the effect of pile-up. The number of pile-up events will be smaller as the pulse resolution time gets smaller. Unfortunately as two pulses gets closer and closer it gets harder to separate them and at some minimum gab between consecutive pulses they can't be separated. Below some minimum resolution time, $\tau_{min}$, pulse pile-up can not be prevented. However, consecutive pulses with a separation between $\tau_{min}$ and $\tau$ can be detected and rejected. The minimum resolution time depends on the detector type, the front-end electronics, and the implementation of the pile-up rejector. Pile-up is only a problem at higher count rates. The pile-up effect is a strong non-linear effect, meaning that it is almost negligible at count rates far below the critical count rate, but leads to a completely messed up spectrum just a little bit above the critical count rate.

## 5.2 X-ray Tube

This section lists all the characteristics of the tube. As already mentioned previously, the tube used is a simple X-ray tube for cardiovascular examinations (Tab.5.3), therefore it has no optical focusing inside and the anode is without any slits, necessary in a CT tube for the heat dissipation and for the expansion. This type of X-tube was used for a preliminary investigation of the effects which we are interested in to reduce the amount of possible variables. This will make it easier to try to divide and trace the different causes of the effects recorded. In the tube used, as seen in the image, there

are two different emitters for the large FS and the small FS and due to the lack of the optical focussing, the anode tracks are different.

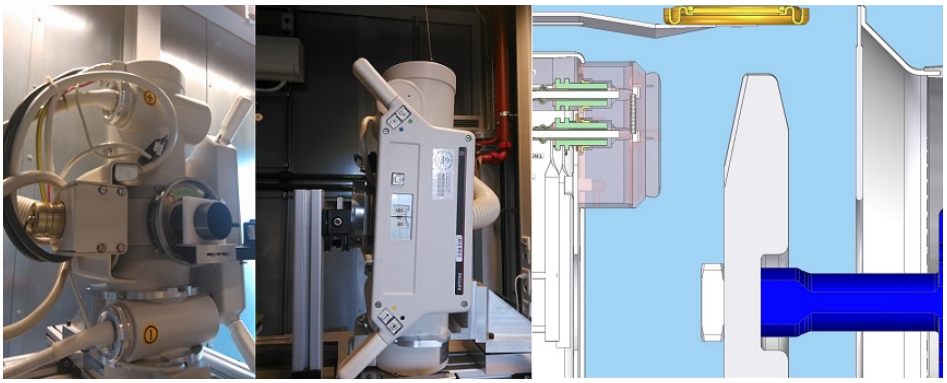

**Figure 5.4:** *SRM 05 11 tube in the laboratory, inside housing.*

The tube used is a high performance SRM 05 11 rotating anode tube integrated into the X-ray tube assemblies SRM 05 11 - ROT 501. Due to the high heat dissipation of the anode and of the large X-ray field (anode angle 11°), this X-ray tube is especially suitable for vascular examination and used in interventional X-ray imaging. Combined with the sharp focal spots, this results in a universal field of application. With its continuous output, the X-ray tube assembly SRM 05 11 - ROT has been specifically developed for high-throughput units. The tube described above is powered by a three-phase generator.

## 5.3 Collimators

The last main things used in the construction of our setup, are collimators. A set of collimators was ordered with its holder, which will be described later. One collimator was positioned in a special-designed tungsten holder positioned close to the tube exit windows. In order to accommodate applications where the X-ray flux is too high for both the detector and the electronics that process the X-ray spectrum, Amptek has developed a "Collimator Kit" to collimate the primary X-ray beam. This system is comprised of the standard XRIO0 1.5 inch extender box which slides inside the EXVC Collimator Housing. The EXVC Collimator Housing can accommodate up to two Tungsten (W) collimator disks that are placed inside a bayonet holder in front of the detector. By selecting the appropriate Tungsten collimator disks, the user can reduce the incoming X-ray flux and allow the detector and electronics to process the X-ray spectrum.

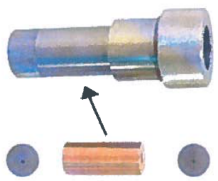

**Figure 5.5:** *Collimators set and holder [3].*

| Disks Collimator(W) | |
|---|---|
| thickness-mm | $\mu$m(d) |
| 1 | 25 |
| 1 | 50 |
| 2 | 100 |
| 2 | 200 |
| 2 | 400 |
| 2 | 1000 |
| 2 | 2000 |

**Table 5.1:** *Disk collimator.*

| Cylindrical Collimator(W) | |
|---|---|
| thickness-mm | $\mu$m(d) |
| 19 | 150 |
| 36 | 300 |

**Table 5.2:** *Cylindrical collimator.*

Seven different Tungsten collimator disks are provided with different size holes in order to allow for a wide range of applications. The EXVC collimator housing is made of stainless steel and can also be used inside a vacuum chamber.

## 5.4 Flat Panel Detector

The flat panel detector has been used for the alignment of the entire system, as will be explained later. It is a prototype model used in research [14]. The only information on the flat panel detectors are the following.

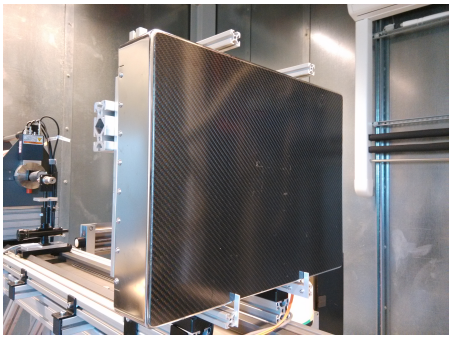

**Figure 5.6:** *Trixell Pixium 4700.*

[14] The detector is a Pixium 4700 and represents a significant step forward in detector technology for high-energy X-ray diffraction. The detector design is based on digital flat-panel technology, combining an amorphous Si panel with a CsI scintillator. The detector has a useful pixel array of 1910 x 2480 pixels with a pixel size of 154 $\mu$m x 154 $\mu$m, and thus it covers an effective area of 294 mm x 379 mm. Designed for medical imaging, the detector has good efficiency at high X-ray energies. Furthermore, it is

capable of acquiring sequences of images at 7.5 frames per second in full image mode, and up to 60 frames per second in binned region of interest modes. The following are the basic properties of this detector applied to high-energy X-ray diffraction. Other properties of the Pixium 4700 detector, including a narrow point-spread function and distortion-free image, provides high-quality diffraction data at high X-ray energies.

| Technical data of the X-ray tube | | | |
|---|---|---|---|
| Type of X-ray tube | SRM 05 11 | Type no.:9890 000 0434x | |
| Manufacturer | Philips Medical System, Hamburg | | |
| Nominal X-ray tube voltage | Symmetrical with respect to groud, 6 and 12 pulse equivalent or DC | 125 keV | |
| Focal spot | Location of focal spot | Superimposed | |
| | Nominal focal spot value | 0.5 | 1.1 |
| Cathode | Maximum filament rating for adaption to X-ray Gen. | 6.62A | 6.54A |
| Anode | Nominal anode input based on | | |
| | 20W equivalent anode input power | 36 kW | 96 kW |
| | 250W equivalent anode input power | 30 kW | 80 kW |
| | 450W equivalent anode input power<br>Maximum heat dissipationi in cont.mode | 24 kW | 64 kW |
| | with non rotating anode | 350 W | 500 W |
| | with rotating anode | 500 W | |
| | Maximum anode heat content | 593kJ | |
| | Maximum anode cooling rate | 3.3kHU | |
| | Anode disk mask | 1000g | |
| | Anode disk diameter | 100mm | |
| | Focal track mask | 85mm | |
| | Target angle | 11deg | |
| Target materials | Rhenium alloyed tungsten; compound anode with molyb alloy | | |
| | Geometrical coverage with SID = 100cm | 39cm · 39cm | |
| | Maximum X-ray field | | |
| | with SID = 70cm | 25cm · 25cm | |
| | with SID = 100cm | 35cm · 35cm | |
| | Accelleration time | 1.4sec | |
| | Anode speed | 8000...10000r.p.m. | |
| Filtration | In terms of quality equivalent filtration by irremovable materials | <0.1mm Al | |

**Table 5.3:** *Tube specification [Reference manual for the SRM 05 11 X-ray tube of Philips].*

# Chapter 6

# Set-up and system calibration

To obtain reliable measurements to analyze the spectrum stability and avoid the alignment and pileup problems, a particular set-up is needed. Here will be explain how this particular set-up was made and all the calibrations measurements will be explained.

## 6.1 Set-up description

This type of experiment required a particular setup (showed in the pictures below 6.1) that was entirely built in the laboratory, specifically to solve and minimize the problems which are listed below:

- reduce the heigh flux;
- align on the same high tube window - collimator - detector;
- create a stable and stiff setup, stable enough for tube operating vibration;
- find an easy way to change the tube position and the tube itself (movable hold for the tube and the collimators).

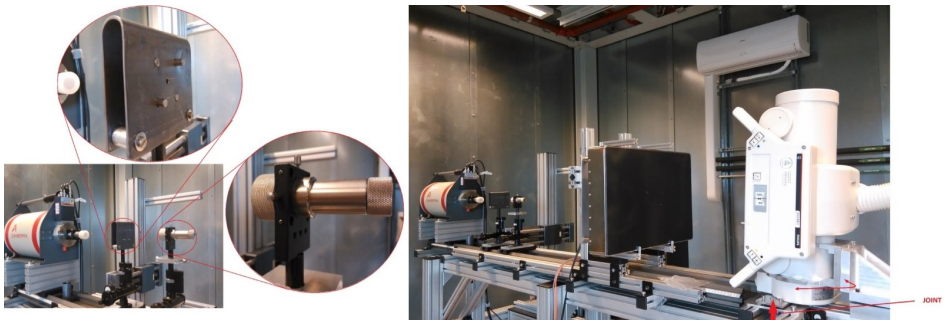


**Figure 6.1:** *Images of the setup.*

The fig.6.1 shows the entire set-up and how it was built. To overcome the problem of stability all the aluminium profiles were fixed on one side while the movable support during the whole experiment was fixed to another laboratory table. The set-up was

designed to be portable once the tube and the detector were removed. The required precision in the alignment of the collimators with respect to the tube and detectors was obtained by positioning all the collimator on the optical bench, with three-directional manually adjustable collimators. The figures 6.1-6.2 shows how many degree of freedom are used in the setup. In addition to the possibility of moving the detector tube and the collimator along the directions $X, Y, Z$ it is also possible to change the $\alpha$ and $\beta$ angles (see Fig.6.3).


**Figure 6.2:** *Images of the collimators holder.*

This made the alignment easier and moving the collimators along the X and Y also allowed us to carry out a scan of the focal spot; the variation of the angle $\alpha$ is needed, as we shall see later, for the alignment of the beam and to make the output beam parallel to the optical bench; the $\beta$ angle, as we shall see in the experimental part, allowed us to investigate and record the spectrum at different tube emission angles. The germanium detector was also fixed on the optical bench to allow for simpler alignment with the rest of the set-up. The height of the focal position of the tube was calculated, so that the collimators and the detector were the same height. This allowed to make a fine alignment only on the position of the collimators. In figure 6.3 the arrangement of the set-up is shown in schematic way and below, in the table 6.1, the distances in the set-up and the dimensions of the collimators are specified.

| | | |
|---|---|---|
| coll. ⊘ | C1 | 200$\mu$m |
| coll. ⊘ | C2 | 300$\mu$m |
| | z | 1680 mm |
| | z4 | 36 mm |
| | z5 | 100 mm |
| R1 | z1+z2 | 140 mm |
| Active detector area | | 100mm$^2$ |
| Focal Spot(F.S.D.) | 0.5mm$^2$ | 1.1mm$^2$ |

**Table 6.1:** *Set-up dimension.*

As explained in section 5.1.2, one of the major problems to be solved is the high count rate. For this reason the aim was to maximize the distance between tube and detector as much as it was possible inside the laboratory; furthermore two collimators

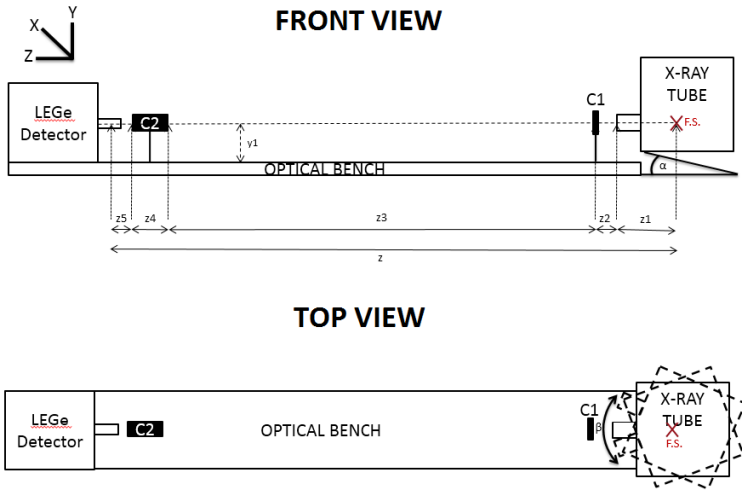


**Figure 6.3:** *Sketch of the whole setup.*

were inserted on the optical bench in order to reduce the X-ray flux (fig.6.3). An alignment process along $X, Y$ and $Z$ was necessary as well as along the $\alpha$ and $\beta$ angle. This was achieved by positioning the blocks on the optical bench according to the data and information (e.g. focal spot position inside the housing) found in the instruction manual and obtain alignment using a precision laser. The measurements obtained by the flat panel detector will be described later in this chapter (section 6.2). This whole process made all subsequent data valid and reliable. In this experiment it was necessary to shield the tube, the detector, and both collimators. This shielding avoided backscatter radiation which could influence and contaminate the spectrum. The next section will discuss the effect of backscatter.

### 6.1.1 Adopted configuration

For this type of experiment, two different types of configurations were used.

#### First configuration

In the first configuration used in the course of the paper, the X-ray tube was tilted of 4° along $\alpha$ angle (fig. 6.3). This inclination of the tube was used in order to be sure that the part of the X-ray beam selected with the first collimator, is the middle and the higher intensity of the focal spot. Moreover the angle in the simulations will be 11° that is, the angle of the anode plus 4°. The collimators used are those described above with the same openness and distances as shown in the image above.

#### Second configuration

Instead in the second configuration the $\alpha$ angle was re-set to 0°; this configuration was used to avoid any kind of problem with alignment of the beam with collimating during the rotation of the tube on the $X, Z$ plane. It's easy to image that the rotation of the tube with the tilted tube, it wouldn't have been so easy. Furthermore with this configuration the measurements with filter material were done, because replacing the first collimator with filter material, the parallelism of the out-coming beam is not

anymore mandatory. Therefore with filtering material, the only difference was the tube angle and the absence of the collimator.

## 6.2 Set-up calibration measurements

Our first approach to this project was theoretical. First of all we estimated by means of geometrical calculations the magnification, and the distance source-detector in our laboratory (tab.6.1) and then new collimators were ordered.

$$M = 1 + \frac{OID}{SOD} \tag{6.1}$$

and

$$\frac{-y_1}{f} = \frac{x_1}{x_3} \tag{6.2}$$

where:

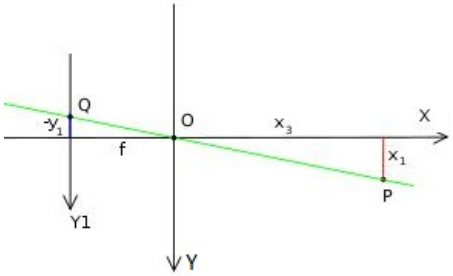


**Figure 6.4:** *In this figure we see two similar triangles, both having parts of the projection line (green) as their hypotenuses. The catheti of the left triangle are $-y_1$ and $f$ and the catheti of the right triangle are $x_1$ and $x_3$ . Since the two triangles are similar it follows the formula 6.2.*

| M | Magnification |
|---|---|
| SOD | Source-Object Distance |
| SID | Source-Image Distance |
| OID | Object-Image Distance |

**Table 6.2:** *Symbol explanation.*

First theoretical estimations were done, then geometrical setup was derived (like magnification ans so on), and then according to the derived geometries new components were ordered. The estimate of the photons, as already mentioned, is the biggest problem with this experiment, so the aim was to reduce the amount of photons emitted by the X-ray tube. This is necessary to reduce the pile-up effect that can happen in the Ultra LeGe detector (see 5.1.2). The intensity of photons emitted by a general tube follows an inverse square distance law. As said before, the problems is to decrease from $5 \cdot 10^9$ $\frac{ph}{s \cdot mm^2}$ in 1mt distance for maximum 1A tube current to $10^4$ $\frac{ph}{s}$ for whole detector area (maximum intensity possible to avoid the pile-up effect); this might seem impossible but it is not, since the focal spot diameter is limited and the spot is imaged according to a hole camera principle. A possible experimental set-up could be a small collimator close to the tube and a second collimator close to the detector (this will be just the first configuration adopted). In our case, using the set-up data from the previous chapter (6.1), with minimal possible current of 10 mA (limited by the generator hardware),

going from 1000mA $\rightarrow$ 10 mA already reduces by a factor of 100, so $\sim 5 \cdot 10^7 \frac{ph}{s \cdot mm^2}$ in 1mt distance remain.

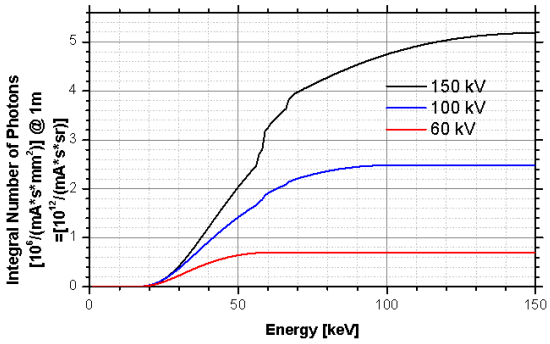


**Figure 6.5:** *Plot for the integral photon intensity.*

There is no clear threshold for the pile up effect in the detector; pile up can occur at any intensity. $10^4 \frac{ph}{s}$ are a "recommendation" limit by the manufacturer, stating that at $10^4 \frac{ph}{s}$ the pile up curve has its maximum. Assuming the first collimator was placed ($C1$) at $R1$ distance to the source, and the second collimator ($C2$) just slightly in front of the detector, the following results were obtained. First collimator with diameter $C1$ enlarges the spot by a factor $\sim$10 using the pin-hole camera equation $\rightarrow \frac{z3}{a} = \frac{z1+z2}{F.S.D.}$ where $a$ is the enlarging factor. So the transmitted intensity ($10 \cdot F.S.D.$=5x5$mm^2$) for large spot distribution on detector area $= 2.5 \cdot 10^{-5} m^2$ = beam area at the detector = $A$ [1]. Transmitted intensity

$$\simeq \pi \cdot \frac{C_1^2}{R_1^2} \cdot J \simeq 6.4 \cdot 10^{-6} \cdot J \tag{6.3}$$

with J = limit value as in above plot, for 100keV $= 2.5 \cdot 10^{12} ph/(mA \cdot s \cdot sr)$. The second collimator filters a part

$$\pi \cdot \frac{C_2^2}{A} \simeq 10^{-3} \cdot J[sr] \tag{6.4}$$

So, after doing all the calculations $\simeq 16000 ph./(mA \cdot s)$ is accumulated. This is already enough, for 10 mA minimal current to reach the pileup regime of the detector, but with the above mentioned experiments, it will be possible to observe the pileup effect and doesn't take into account. Once these two different types of estimates were completed, we went back to the practical work in the laboratory to try to build a precise set-up, in order to obtain accurate and acceptable measurements. First of all, the alignment had to be divided into various sections. Since various set-up were possible (a lot of degrees of freedom were present), as shown in the previous chapter, we had to make sure that the whole system was correctly aligned. The first step, was a rough alignment. In this set-up the focal spot point on the anode (as specified in the manual), the collimators on the optical bench and the Ultra LeGe detector were all positioned at same height. Of course the first alignment measurements were made in an approximate way. The next step was to build a support for an extremely accurate optical laser to be used for more precise alignment. Once the optical laser was put into position, the alignment was still not complete; the position of the detector was not a

[1] see tab. 6.1 for symbol

problem since its sensitive surface was large enough, instead care had to be taken with the position of the collimators. They were placed such that collimator holes and focal spot were crossed by the optical axis. This was not easy to achieve. The collimators have a variable diameter between 25 $\mu$m and 300 $\mu$m (the list of all the dimensions is provided in the previous chapter) and the latter has a length of more than 36 mm. The main difficult was to align the collimeter and the whole system to a cavity of 300 $\mu$m with a length of 36mm.
In the meantime a holder was built for the existing flat panel detector in the laboratory. This kind of detector was used for all the final precise alignments. The first measurements were taken by removing all the shielding in front of the X-ray window and measuring the angular extension of the X-ray beam passing the beryllium window, in order to check how the beam was emitted and if the focal spot is centered on the optical axis. This kind of information was necessary because the first collimator C1 selects only a small part of the focal spot point on the anode, so it was necessary to know which part was selected. The only way to know this, was to analyse the emitted beam with the flat panel detector and compare its position with the lighted pixel from the beam which had gone through the first collimator. The first result was the intensity profile along the Y direction (see fig.6.3 for the coordinate system).

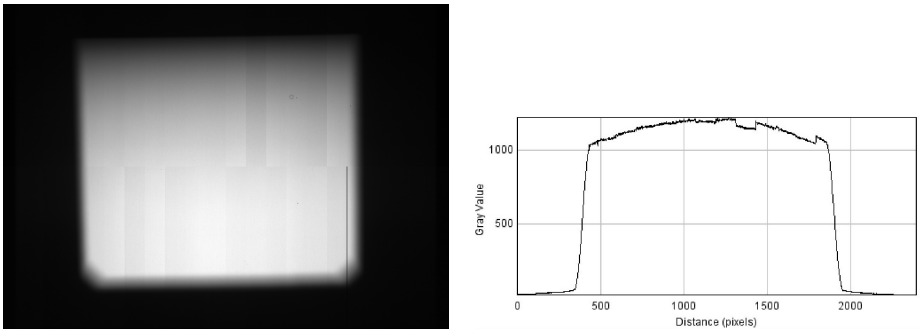


**(a)** *Image with the Flat Panel Detector of the whole beam.*

**(b)** *X symmetric profile.*

**Figure 6.6:** *Whole beam and his intensity profile along X.*

Here the result was a image with a greater intensity, in the lower half of the detector. The data collected from the flat panel detector were row data taken directly without any gain correction. This was done because the level of precision required was not high and because these measurements were used just to align the whole system. As it is possible to see in the image 6.6*b*, the profile along the X direction is quite symmetric, but is asymmetrically along the Y direction. This could be explained by three different factors:

- the square-distance law and the non-perpendicular incident angle;
- different gain or a simple effect of the detector;
- the Heel effect.

The hypothesis of different gain due to different zone can be reject straight away because if this had been the case the changing in the intensity would have been sharper,

as can be seen in a constant way along the X direction (see fig 6.6*b* )[2]. Therefore the first step was to elaborate these acquired images, with a geometrical correction. The Heel effect was not taken into consideration, at least for these first calculations, considering that the beam had an isotropically emission and so the emission angle of $I_0$ was constant[3]. According to these assumptions:

$$I(x,y,z) = I_0 \cdot \frac{1}{r^2} \cdot cos\left[\alpha\left(x,y,z\right)\right] \tag{6.5}$$

with $r^2 = x^2 + y^2 + z^2$ where $\frac{1}{r^2}$ is due to the *square distance low* and $cos\left[\alpha\left(x,y,z\right)\right]$ due to the *"not perpendicular incident angle"*. So for the trigonometric laws $cos(\alpha) = \frac{z}{r}$ and by replacing 6.5 with this we have:

$$I(x,y,z) = I_0 \cdot \frac{z}{(x^2+y^2+z^2)\cdot(x^2+y^2+z^2)^{\frac{1}{2}}} = I_0 \cdot \frac{z}{r^3} \tag{6.6}$$

Matlab was used to correct the acquired emission for these factors and the result was the following Y profile. After this correction it is possible to say that the effects seen in the images are due only to the heel effect. After processing the images, the profile after has reached the maximum height, doesn't not decrease anymore as in fig.6.7*a*, but continue to raise (fig.6.7*b*); this is a symptom of the Heel effect and removal of the effect due to the square-distance low and the non-perpendicular incident angle. After this correction these results can be considered reliable so, the next step to consider will be alignment.

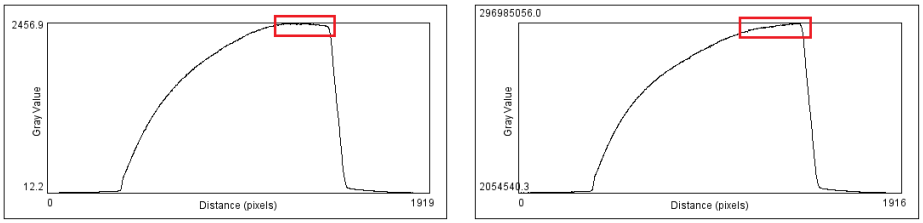


**(a)** *Profile before geom. correction.* **(b)** *Profile after geom. correction.*

**Figure 6.7:** Y profile of the whole beam. The intensity decline towards one edge is due to heel effect, intensity decline towards other edge is due to the collimator shadow (blurred by the penumbra of a finite spot size).

After this type of correction for all the images taken with the flat panel detector, some images were acquired without any collimation and shielding in order to obtain the while profile of the emitted X-ray beam. The flat panel detector was placed in different positions along the optical bench with different distances (reported on tab. 6.3 ) from the focal spot. In this way, it was possible to compare the different images and come up with the position of the focal spot related to the position of the first collimator.

As it is possible to see from the intensity profiles and the table 6.3, no problem was found along the X direction, but it seemed that the center of the cone beam did not remain at the same Y (high from the optical bench) for all the path, from the tube

[2]It is possible to see the different zones with different gain, with the sharper change in the intensity profile.

[3]In formula 6.5 it is possible to simply account for the heel effect by making $I_0$ angular dependent

| Distance(mm) | Center PXL(X) | Center PXL(Y) |
|---|---|---|
| 210 | 1281 | 1092 |
| 245 | 1280 | 1102 |
| 285 | 1280 | 1116 |
| 365 | 1278 | 1140 |
| 410 | 1277 | 1151 |
| 440 | 1277 | 1165 |

**Table 6.3:** *Position of the center pixel of the whole beam on the flat panel detector, changing the distance, moving the detector farther from the focal spot.*

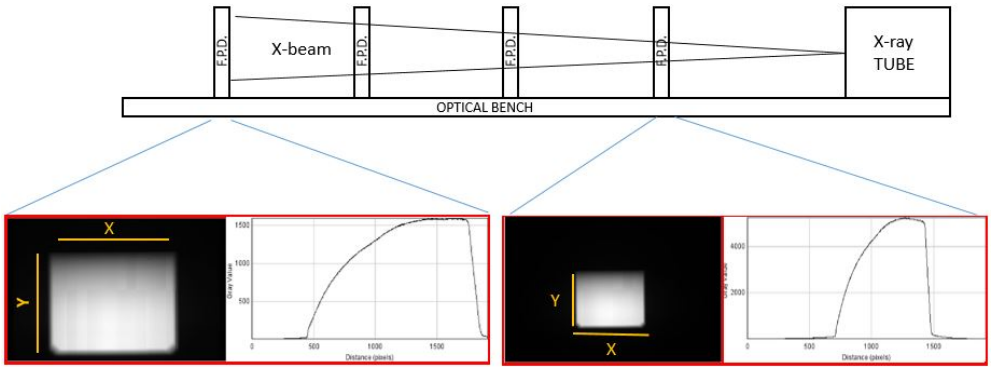


**Figure 6.8:** *Sketch of the flat panel detector position during the calibration measurements. X = center pixel along the X direction. Y = center pixel along the Y direction.*

to the detector. The table indicates that the X-ray tube had to be rotated slightly to be sure that the position of the collimator hole was aligned to the center of the focal spot. This meant that by doing a simple calculation it is possible to identify the position of the pixels corresponding to the center of the focal spot at each detector position. The tube was rotated so that the position of the central pixel, corresponding to the center of the beam, was always in the same pixel. This data was used later to align the two collimators at this central point. Naturally in this way alignment with the rotation axis with the focal spot was lost, so with this kind of configuration, only measurements without rotating the tube were recorded. This choice was made because the purpose of the measurements required was to indicate the precision of the system and the reliability of future measurements, so the objective was to minimize all external factors (i.e. the issue of the beam not being parallel to the optical bench).
After this adjustment, the flat panel detector was positioned as close as possible to the Ultra LeGe detector and some images were acquired by moving the collimators on the optical bench. The main purpose of the operation was to maintain the same area illuminated by the beam passing through the collimator. Once this issue was settled , attention was shifted onto aligning the longest collimator. In this case no automatic support was available, so the rotation and the manual adjustment was done by screws. The collimator was placed in front of the flat panel detector and some images were recorded in order to find the position of the collimater that transmitted the highest intensity image. Finally, the last step, was to align the two collimators, one at the exit of the window of the X-tube, with the other in front of the germanium detector. Again,

the flat panel detector was used and placed in close proximity to the counting detector. Images has been acquired with a single collimator each time and its position has been adjusted so that the pixels illuminated corresponded to the same pixels previously calculated.
This concludes the explanation of how the configuration set was achieved from which all the measurements explained in the next chapter were taken.

# Chapter 7

# Experimental measurements

All the spectra recorded will be illustrated and compared in a quantitative way, but for the most interesting aspects, it will be possible to compare qualitative aspects with the normalized spectrum[1] and total counts as well. More detailed analysis will be done on the temperature measurements and all explanation can be found in the relative chapters.

## 7.1 First set of measurements

The first priority was to investigate the stability of our system and its range of operations and establish the error margin of all obtained results, to understand the reliability of future measurements. Below is a list of preliminary measurements recorded, to accurately establish this data:

- stability over time (same measurements, same conditions, different days)
- scattered radiation
- detector noise and dark image
- number of X-ray pulses (how and if they influence the measurements)
- stability throughout a working day (2 min and 15 min between one and another)
- temperature test
  - room temperature vs maximum anode heat capacity
  - heating and cooling process
- pile-up check

### 7.1.1 Stability over time

This first kind of investigation done, was to evaluate the stability of the system over different days. Same measurements were recorded with totally identical parameters on different days, and the same condition were reproduced every day and nothing in

[1] Normalized spectra = spectra where each beam has been divided for the total count of the whole spectra and the difference it is just the difference bin by bin.

the set-up between one measurements and another was changed. The absolute spectra and the differences in normalized spectra and the list of the entries for each day are shown below. From the images 7.1 and the table 7.1, spectra looks stable and it is impossible to see any reproducible pattern in figure 7.1($b$). This mean that the only difference is caused by statistical deviations. Instead for the counts there are some not negligible effects. The effect seen in the counts are not inside the deviation of square N, and could be caused by everything (e.g. a small movement of the equipment from a day to another). For this reasons the next comparisons will be done with the normalized spectra instead the absolute one. So, the conclusion is that it is possible to compare normalized spectra taken on different days but always paying attention when comparing absolute spectra.

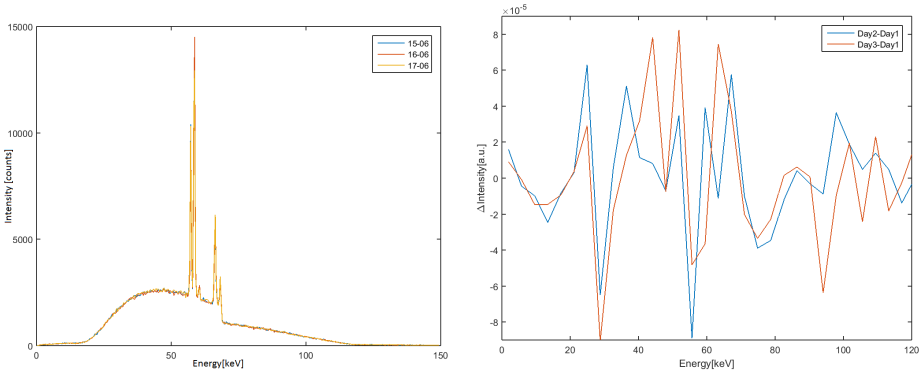


**(a)** *Spectra taken on three different days.* **(b)** *Difference in normalized spectra.*

**Figure 7.1:** Spectra taken on 3 different days

| Days | Tot.Counts |
|---|---|
| day 1 | 398561 |
| day 2 | 393771 |
| day 3 | 400310 |

**Table 7.1:** Counts for spectra taken on 3 different days.

### 7.1.2 Scattering radiation

Obviously the X-ray beam is strongly collimated and this significantly contributes to creating a high percentage of scattering and backscattering radiation. These particular measurements were taken to quantify the influence of this radiation on our spectra and evaluate the efficiency of the shielding. These images were taken with two particular tube settings (100 kV 10 mA 20 sec and 120 kV 100 mA 10 sec), putting 6 mm of lead in front of the opening of the pinhole collimator close to the detector during acquisition. The duration of acquisition was the same as used for the previous spectrum measurements shown in fig.7.1. In this way, the main beam was blocked and just the scattering radiation was recorded. The results show us how shielding works with the two different settings. Obviously, increasing the mA, increase the quantity of scattered

radiation detected, but for exactly this reason it doesn't matter which mA to be used since the relative error induced by scatter is independent of mA.

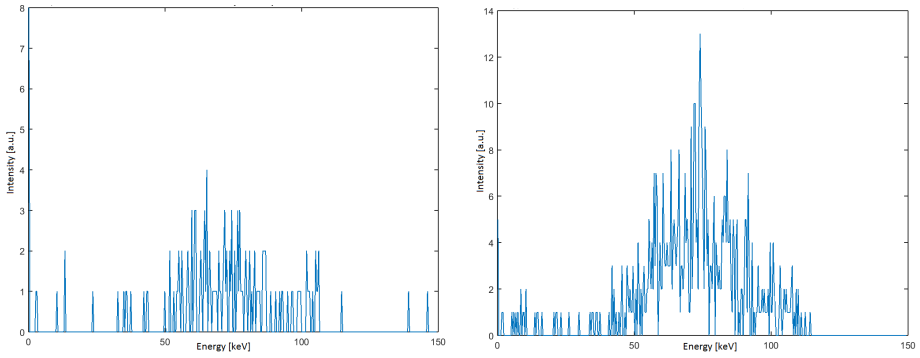


**(a)** *Scatt. rad. 100 kV 10 mA 20 sec.* **(b)** *Scatt. rad. 120 kV 100 mA 10 sec.*

**Figure 7.2:** Scattering radiation spectra.

| | Counts |
|---|---|
| Scattering (a) | 153 |
| Scattering (b) | 548 |

**Table 7.2:** Scattering radiation counts.

The reason that we reduce the mA, is only due to pile-up. If we hadn't pile-up, we would increase the mA as much as possible to reduce statistical error. The scatter-to-primary ratio $\% = (\frac{Scatt.Counts}{Tot.Counts}) \cdot 100$, was the formula used for a simple calculation of the influence of the scattering radiation on the total counts of the whole spectrum. Taking the two extreme cases as counts of the analysed spectra, which are 75000[2] and 300000[3], using the formula above, the results are 0.6% and 0.2% respectively. Comparing these calculations with the next type of measurements and its magnitude, it cannot be considered the dominating sources of error for this experiment.

### 7.1.3 Detector noise and dark spectrum

In this evaluation, two different kinds of measurements were taken. Both of them were a sort of dark image for a flat panel detector; the first one was taken with all the acquisition equipment (tube and HV generator) turned ON, while the second one with all the equipment turned OFF. Only one measurement is illustrated because as can be seen from the table, the counts of the two configuration modes were more or less the same. As before, the counts of the analysed spectra range from 75000 to 300000; this means the counts obtained with the tube OFF, affect the spectrum with a rate of 0.05% to 0.01%. As for the scattering radiation this effect cannot be considered the dominating sources of error for this experiment.

[2] C1=200$\mu$m, 10mA, 100keV, large focal spot
[3] C1=400$\mu$m, 10mA, 100keV, small focal spot

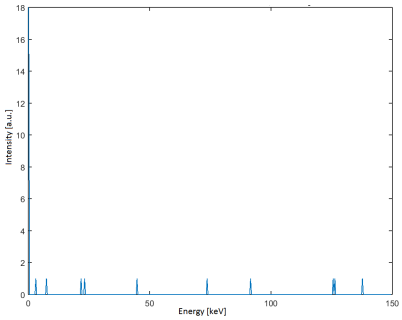


**Figure 7.3:** *Dark image taken with all the instruments ON.*

| | Counts |
|---|---|
| Dark1 | 39 |
| Dark2 | 28 |

**Table 7.3:** *Photon counts. Dark1 was taken with the equipment ON. Dark2 was taken with the equipment OFF*

### 7.1.4 Rising and falling edge of the generator pulse

The generator applies voltage pulses to the tube and these pulses are affected by ripples and the rising and falling edges are not ideal step. For an ideal reference spectrum, the generator needed to provide a "*continuous mode*", but, as explained in the generator description in chapter 5, this was not available, so we had to operate just in "pulsed mode".

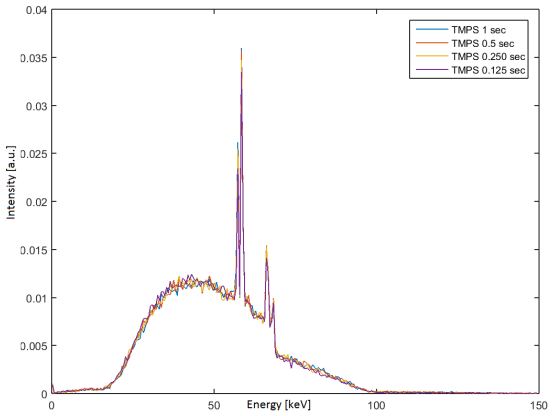


**Figure 7.4:** *Spectra taken with same exposure time but different number of pulses with different duration (TMPS)*

| N. Pulse | TMPS(sec) | Counts |
|---|---|---|
| 10 | 1 | 75550 |
| 20 | 0.500 | 75692 |
| 40 | 0.250 | 75221 |
| 80 | 0.125 | 75694 |

**Table 7.4:** *Photon counts.*

For these reasons, in one of the following chapter, the HV signal taken directly from the generator will be illustrated whereas in figure 7.4 some spectra with a different number of pulse are shown. The pulse duration was adapted such that the total exposure time was constant for all spectra. The same amount of counts was expected and the results confirmed the expectations within the statistical noise of 500 counts. So the conclusion is that the spectra are not dependent on the number of pulses applied during a particular exposure time.

### 7.1.5 Stability throughout a working day

After analysing the same measurements taken on different days under the same conditions as mentioned in section 7.1.1, the attention was put to the stability of spectra with time.

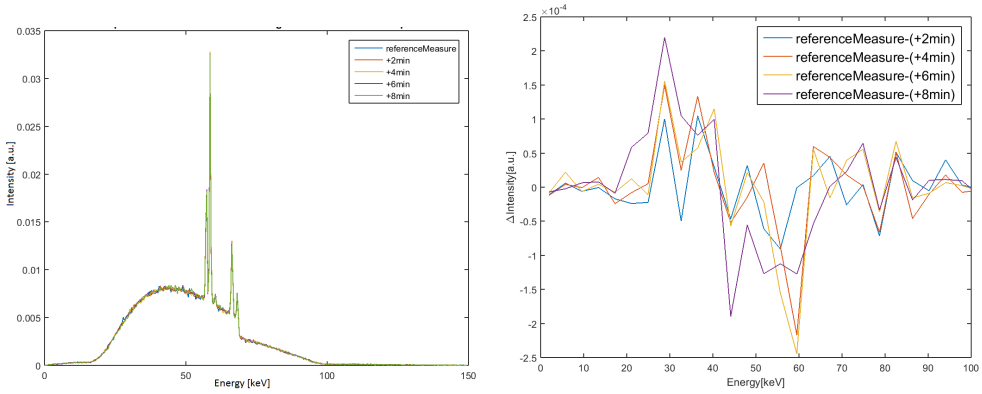


**(a)** *Norm. spectra 100keV 10mA 20sec.* **(b)** *Diff between reference norm. spectrum and the other one.*

**Figure 7.5:** Time between each acquisition: 2 minutes

So, the stability of the same measurements taken after a lapse of a few minutes between one and the other (2 minutes and 15 minutes) under the exact same condition was analysed; without changing anything in the set-up and without opening the cabin door either. The spectra and the parameters used are illustrated in fig 7.6.

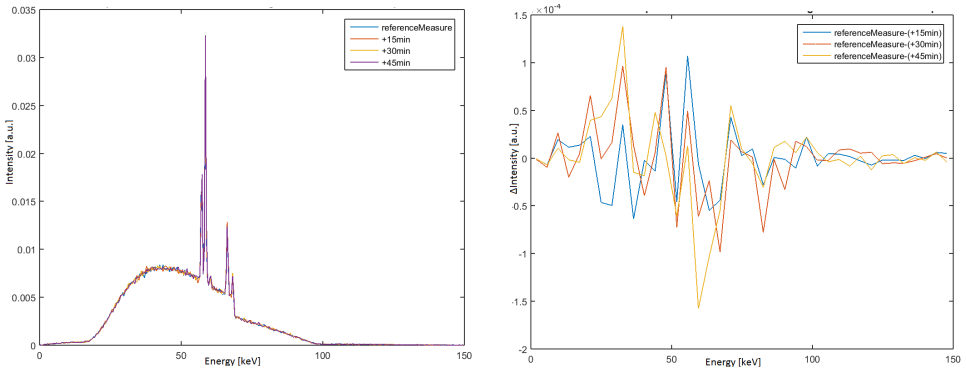


**(a)** *Norm. spectra 100keV 10mA 20sec.* **(b)** *Diff between reference norm. spectrum and the other one.*

**Figure 7.6:** Time between each acquisition:15min

The difference spectrum (2 min) shown deviations up to $2 \cdot 10^{-4}$ as compared to $8 \cdot 10^{-6}$ in section 7.1.1; for this reason it's clear that difference come up with fast sequence measurements. It's also possible to see a recognizable pattern that become evident in the following measurements section during the heating of the tube. Contrariwise the difference spectrum (15 min) shows a little bit less effect in the

magnitude ($2 \cdot 10^{-4} \rightarrow 1 \cdot 10^{-4}$ ), but without a clear pattern as in fig. 7.5. Differences in total counts where evident between the series of measurements taken with 2 minutes and 15 minutes from each other. In the second case, the counts were completely comparable, whereas the first set of data shows an interesting increase in the counts from one to the other and this increase is quite constant.

| | Counts |
|---|---|
| Ref | 300813 |
| +2mins | 302917 |
| +4mins | 304984 |
| +6mins | 308190 |
| +8mins | 311986 |

**Table 7.5:** *Spectra counts.(2 min)*

| | Counts |
|---|---|
| Ref | 301023 |
| +15mins | 300547 |
| +30mins | 299811 |
| +45mins | 301131 |

**Table 7.6:** *Spectra counts(15 min).*

This effect could be due to the behaviour that will be illustrated in the following chapter during the heating of the anode and the whole tube. Therefore, this clearly indicates that, if the purpose is to compare measurement with quite a long exposure (30-40 sec), the anode heating must be kept under strict control. At the same time, it is safe to say that we can compare measurements taken on the same day, but with a long enough interval between them to allow the tube to cool. Obviously the time needed to cool the tube strictly depends on the tube load, i.e. the product of mA and exposure time.

### 7.1.6 Pile-up check and generator sensitivity to the software input

This chapter aims to verify the impact of the pile up effect on our measurements, and check the sensitivity of the generator from the software input.

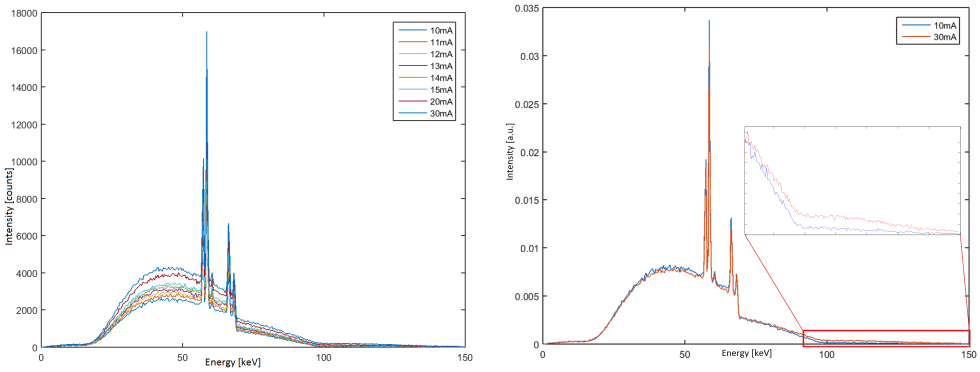


**(a)** *Spectra.* **(b)** *Normalized spectra.*

**Figure 7.7:** Difference between 30 mA and all the other settings for 100 keV

Two series of measurements were recorded, but here only the second one will be analysed because during the first series the temperature of the anode increased as shown previously, so the possible pile up effect could have been modified by the rise

in temperature. During the sequence of measurements, increasing the mA and before finish the sequence, the maximum heat capacity of the tube was reached. For that reason, to avoid the possibility to analyse measurements affected by temperature change, just the second set of measurements was taken into account. This shrewdness was done in order to have the same tube temperature (max.heat) for all the measurements in the set (From 30 keV to 10 keV). From the absolute spectra it was evident that the generator was even sensitive to an increase of 1 mA, in fact it is possible to see different counts and different spectra with each mA increase. Moreover, the effects of the pile up were calculated in two different ways; the first one was simply to compare the normalized spectra. The other way of analysing the pile-up was to evaluate the increase of the counts between 10 and 11 mA and relate this value to the respective increase from 10 to 30.

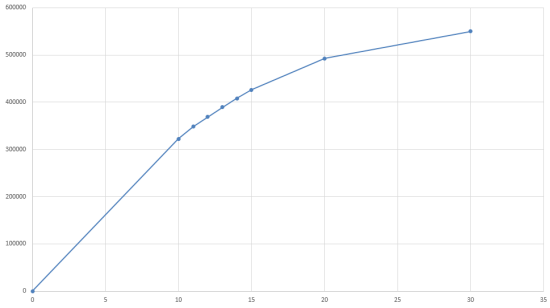

**Figure 7.8:** *Detected counts versus mA (30 down to 10).*

The non-linear plot of the detected counts versus mA indicates we are already in the pile up regime. No limit value can be established from this plot, but it is quite clear that above 10 mA the pile-up effect becomes predominant and create some problems for the measurement of reference spectra. However the effects recorded for this mA are not that strong, so it is possible to prevent them and make some correction, at least for measurements for 10 mA. Another interesting thing to observe, is the plot of differences between the normalized spectra from 30 to 10 mA.

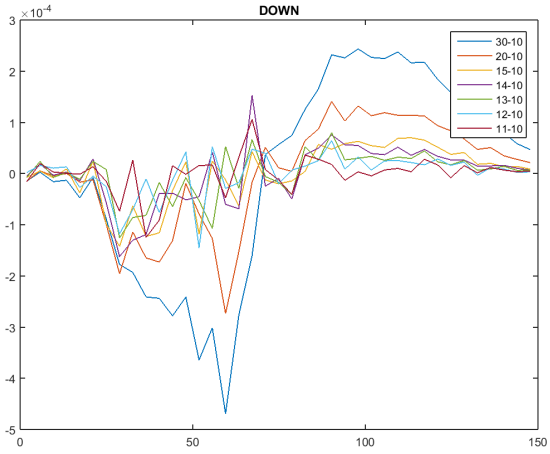


**Figure 7.9:** *Difference between normalized spectra.*

In fig. 7.15 each curve represents the differences between the 30 mA spectrum and

all the others. The result is simply the pile-up effects. What happens with this effect is that the counts are transferred from lower energy to higher energy. Here in fact (7.15) illustrates that below 70 keV there are less counts due to the pile up effect with high mA and above 70 keV there is a much higher number of counts for the 30 mA. This means that some counts are lost for the dead time of the detector and more high energy counts are recorded due to the pile up effect.

## 7.2 Tube measurements in hot and cold condition

After recording some calibration measurements, attention shifted to the main purpose of the project with some interesting results for Philips studies. The reaction of the tube was studied at different temperatures and some relevant differences became apparent.

### 7.2.1 Spectra for a cold and hot anode (first configuration).

First of all the spectra of the cold tube (after 20 hours of inactivity) and the hot tube were recorded and compared. Experiments are usually carried out with 10 mA, however with this settings, according to the rating chart in the Appendix, it was impossible to heat the tube to the intended temperature. Therefore between one measurement and another 200 mA were loaded for 5 sec; to ensure that the measurements taken after this blast occurred at maximum anode temperature.

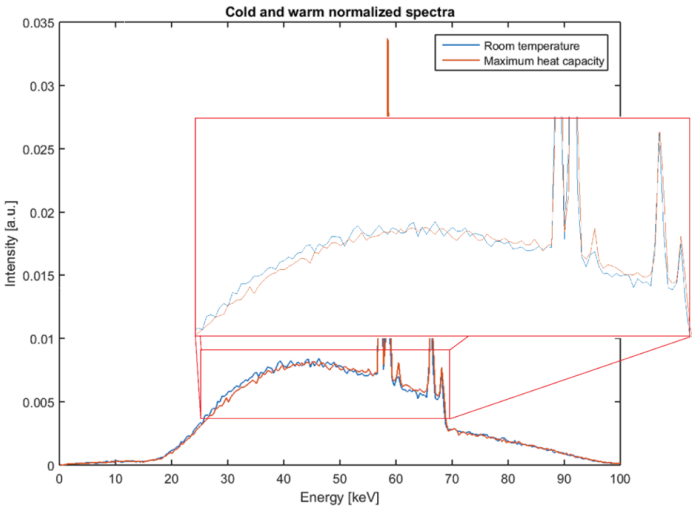


| | Counts |
|---|---|
| Cold | 299312 |
| Warm | 324774 |

**Table 7.7:** *Total photon.*

**Figure 7.10:** *Spectra for a cold and a hot anode.*

The same experiment in the same operating condition was repeated for three different days to give evidence that this results were reproducible. All this measurements were recorded with the small focal spot and with the first 200 $\mu$m collimator to avoid pile-up; this intended set-up to avoid the pile-up select just a small part of the spot ($\sim 180\mu m$ see fig.6.4). The Fig.7.7 indicates the normalized spectra at 100 kV with the respective counts; spectra were also recorded for 80 and 120 kV and are analysed in fig.7.12. Analysing in a quantitative way the results, an increasing in total photon count is clearly evident. A clear difference is also evident in a qualitative analysis of

the normalized spectra. Below 45 keV the spectra taken at room temperature has a number of total photon higher then the spectra in hot condition, while above 45 keV this trend is reversed. In these operating condition a change in position of the focal spot could occur due to the temperature and the optics inside the tube. Considering the small selected area, the difference seen in fig.7.7, could be caused by this focal spot movement. At the beginning it was thought that the small focal spot would have a bigger deviation between the two temperature condition while the large one would demonstrate less deviation due to the larger surface area in question. It is possible that the effect seen on the small focal spot could depend on the movement of the focal spot caused by the temperature. The area lit by the electron beam could consequently be different and the spectrum generated could be different. For this reason, the idea was to repeat the experiment using a large focal spot. In this condition the spectra obtained should be influence less by the movement of the focal spot. This was checked using the measurements below, and the same spectra both for the large and the small focal spot. The comparison between the large and the small focal spot helped us to understand the causes of this effect. The difference between the normalized spectra recorded in hot and cold conditions is plotted below, comparing the large with the small. Obviously the configuration with the mA and the collimators are the same, so for the large FS, fewer counts and more noise have been recorded, since the X-ray flux density is decreased while spreading the focal spot over a larger area. Later in this report it will be possible to see how to achieve the same counts for both focal spots.

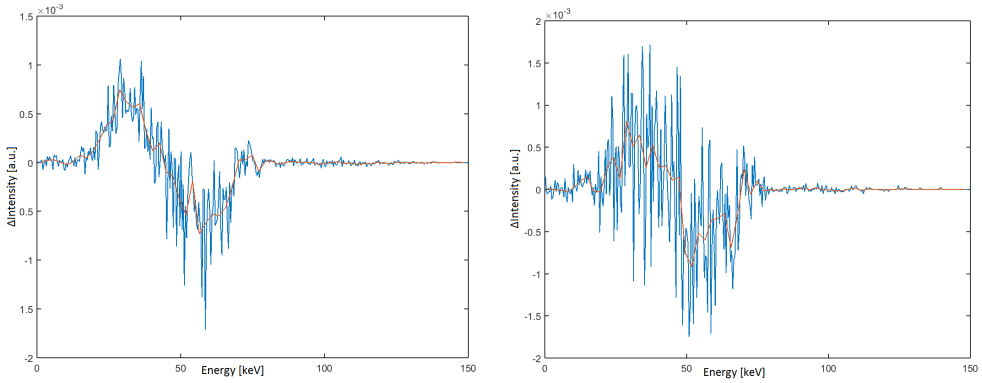


**(a)** *Small F.S.* **(b)** *Large F.S.*

**Figure 7.11:** Difference between hot and cold tube (normalized spectra)

The hypothesis that the focal spot position is moving on the anode surface selecting a different and more area with different roughness can be discarded because even with a more averaged surface (large focal spot) the same trend is still evident. The results of this experiment confirm the same deviation for the small and the large focal spot. Another thing to rule out is that this trend is due to a simple detector effect (pile up). If the measurements used in the experiments in the previous chapter are taken into account, the hypothesis of a pile up problem must be discarded. Furthermore results were also recorded with the small and large focal spot for 80-100-120 kV. The voltage dependency was plotted on the same diagram to show that the trend was always the same and the turning point was always around 48 keV. After comparing this three tube voltage further testing was done at all energy levels which confirmed that the trend doesn't depend on the energy. Therefore any further experiments can now be

done using just one setting.

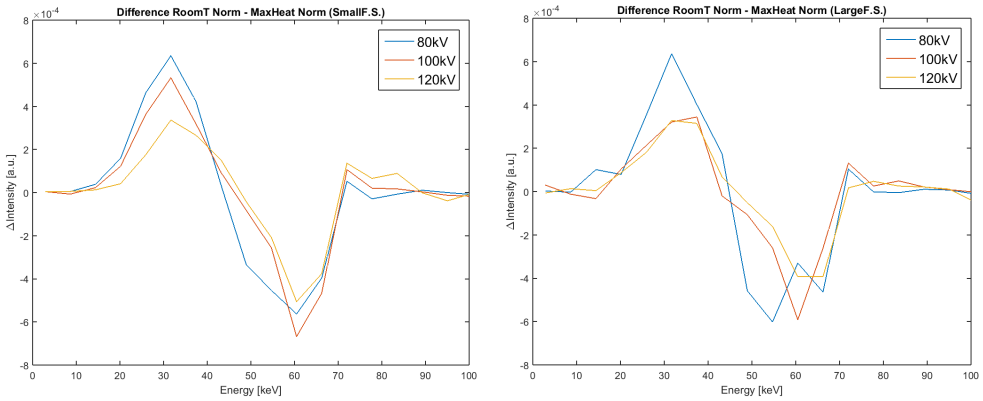


**(a)** *Small F.S.* **(b)** *Large F.S.*

**Figure 7.12:** Difference between hot and cold tube (normalized spectra) for (80-100-120)kV

The results obtained, show that by increasing kV, the effect is reduced but is still very evident (due to the normalization less effect at 120 kV setting is visible because the absolute counts goes up to 120kV). Therefore the conclusion is that this trend is due to some intrinsic change of the anode or cathode.

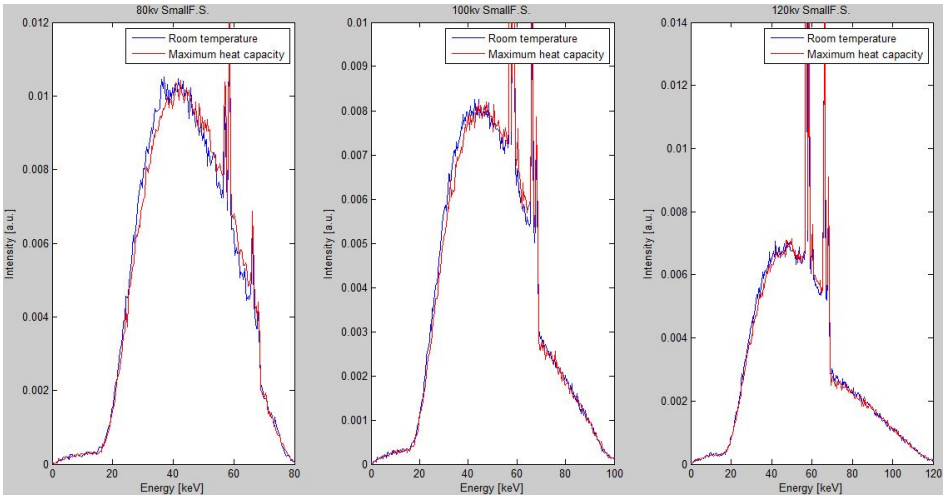


**Figure 7.13:** *80-100-120 keV cold and hot anode.*

After checking that there is no connection between the kV and the effect seen caused by the temperature change, the configuration of small focal spot and 80 kV was selected and some spectra were recorded at different times in hot and cold condition.

These are the settings used to heat the anode and the waiting times during the cooling cycle. Between each setting printed in the table 7.8, a spectrum of 80 kV 10 mA of 20 sec was recorded. In fig. 7.14, only a few steps have been reported to keep it simple. The trend found before, is confirmed. Before 45 keV the "cold" spectrum is above the "hot" one and after 45 keV the opposite happens, but this change in trend

| mA | keV | TMPS (sec) |
|---|---|---|
| 100 | 125 | 1 |
| 100 | 125 | 1 |
| 100 | 125 | 1 |
| 125 | 125 | 3 |
| / | cooling 20 min | |
| / | cooling 40 min | |
| / | cooling 60 min | |
| / | cooling 80 min | |
| / | cooling 140 min | |

**Table 7.8:** *Operating mode where "cooling time" mean the waiting time between two measurements.*

always happens at the same keV (48 keV).

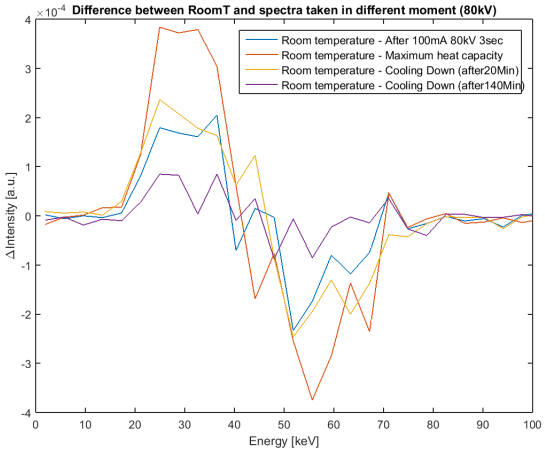


**Figure 7.14:** *Difference between normalized spectra during the cooling and heating processes.*

From this graph it's interesting to see how the trend is completely symmetrical, i.e. during heating this difference increases until it reaches its maximum point when the tube is at its hottest, then the difference decreases until it becomes irrelevant for the spectrum acquired after 140 minutes (the time it takes for the tube to get back to the starting temperature).
After checking the behaviour and analysing in detail the small focal spot, an attempt was made to increase the counts and therefore the statistics for the large focal spot. This was done in two ways: in the first case the opening of the first collimator was increased from 200$\mu$m to 400$\mu$m while in the second case the same collimator was used and the mA increased. After analysing the profile of the focal spot (section **6.4**), the collimators was positioned at the greatest intensity point. This was done to have further confirmation of the behaviour of the tube during heating and cooling.

The following table illustrates the results obtained for the three different spectra divisions, to highlight the behaviour of the tube at different temperature. The first thing that becomes evident from the data is that for the 400$\mu$m collimator at 10 mA the temperature effect is much lower than at any other setting.

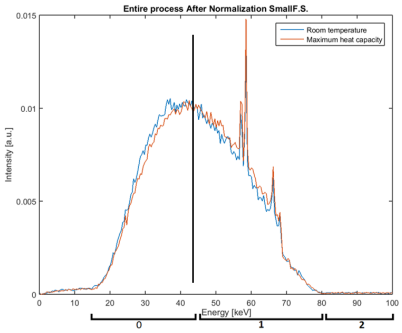


**Figure 7.15:** *Partition of the spectrum (bin in the table), to highlight the differences in a better way. As explained here, the spectrum was divided into 3 different bin, from 15 keV to 45 keV (bin 0), form 45 keV to 80 keV (bin 1) and the last part to check the pilu-up (bin 2).*

| **SMALL FOCAL SPOT** | | | |
|---|---|---|---|
| | **10 mA** | | |
| | collimator 200$\mu$m | | |
| bin | cold % | warm % | Δ% |
| 0 | 0,5191 | 0,5034 | **1,57** |
| 1 | 0,4664 | 0,4809 | **-1,45** |
| counts | 185K | 200K | **-15K** |

**Table 7.9:** *Differences due to the temperature for the different acquiring condition for the small focal spot.*

| **LARGE FOCAL SPOT** | | | | | | | | | |
|---|---|---|---|---|---|---|---|---|---|
| | **10 mA** | | | | | | **20 mA** | | |
| | collimator 200$\mu$m | | | collimator 400$\mu$m | | | collimator 200$\mu$m | | |
| bin | cold % | warm % | Δ% | cold % | warm % | Δ% | cold % | warm % | Δ% |
| 0 | 0.5214 | 0.4962 | **2.25** | 0.5010 | 0.4957 | **0.53** | 0.4983 | 0.4798 | **1.85** |
| 1 | 0,4690 | 0,4952 | **-2,62** | 0,4839 | 0,4897 | **-0,58** | 0,4886 | 0,5094 | **-2,08** |
| counts | 41K | 37K | **4K** | 183K | 181K | **2K** | 106K | 73K | **33K** |

**Table 7.10:** *Differences due to the temperature for the different acquiring condition for the large focal spot.*

By selecting a larger part with a 400$\mu$m collimator instead of 200$\mu$m one, the effect was weaker, averaging and less visible. For this reason in the next paragraph 7.2.2 will be analysed a new configuration without the first collimator, to see if the effect could be a local effect generated by the small area selected by the collimator C1. Another factor that becomes clear from the table is that with a 200$\mu$m collimator at 20 mA the difference in percentage is higher. In the table it can be seen the trend is constant (as regards the normalized spectrum). In the first bin examined the difference is positive, while in the second one it is negative, but it is interesting to note that in absolute count the trend is completely the opposite between the small and the large FS.

### 7.2.2 Spectra for a cold and hot anode (second configuration).

After recording all the measurements listed in the previous paragraph 7.2.1, the idea was to test a different kind of set-up, changing the operating conditions. The purpose was to analyse the spectra in as many different ways as we could, in order to understand the causes of the effects better and try to separate them. The configuration adopted for the following measurements was described in the previous chapter 6.1.1. Just as a reminder, this configuration has the angle $\alpha = 0°$ (see fig. 6.3 for the angle). Therefore, changing the $\alpha$ angle meant the anode angle was -7° and this will be fundamental for the simulation in the following chapter (8).

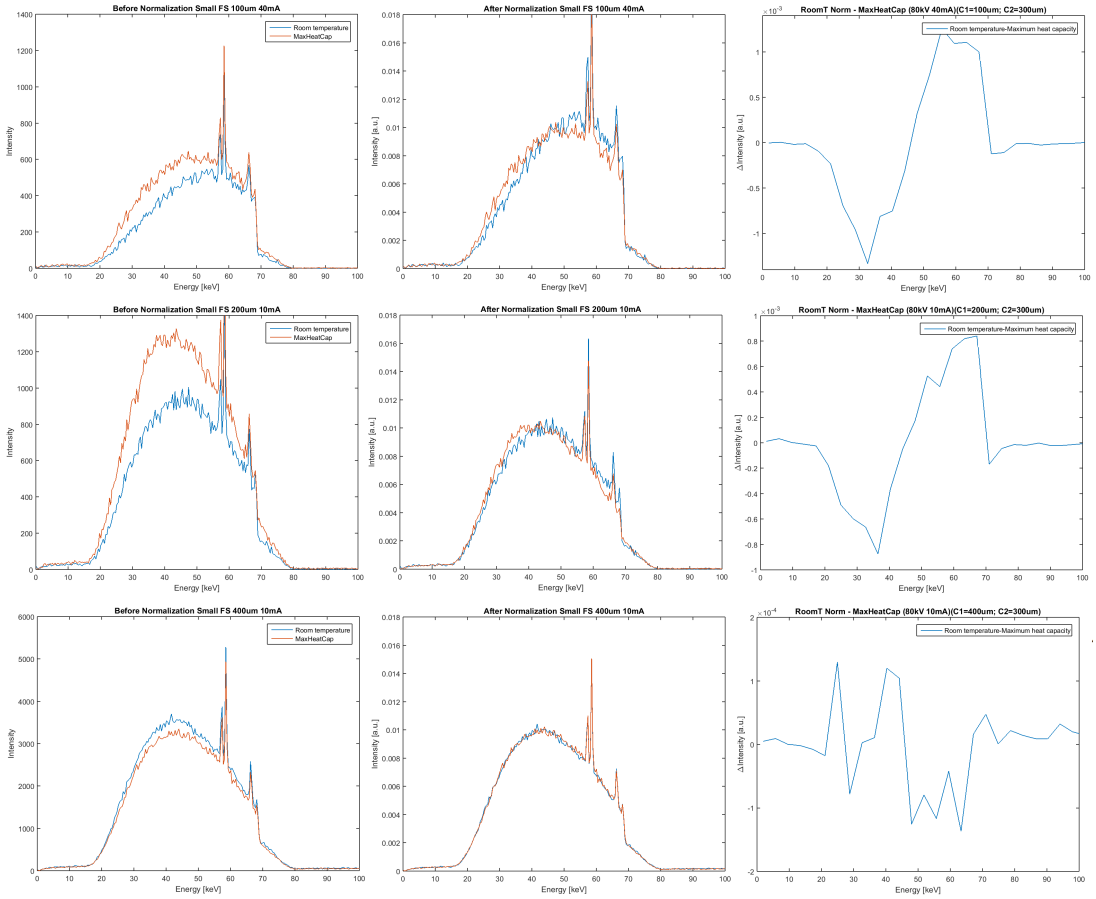


**Figure 7.16:** *Spectra for cold and hot anode conditions at 80 kV. Top row: 100 µm collimator, 40 mA (40 mA were loaded, to increase the flow, the counts, and avoid the noise in order to have the total counts similar for each of them); middle row: 200 µm collimator, 10 mA; bottom row: 400 µm collimator, 10 mA.*

The two set-ups used in this second configuration were:

1. collimators
    - 100 $\mu$m
    - 200 $\mu$m

- 400 $\mu$m

2. filtered material
   - Gd filtration (0.5mm)
   - Cu filtration (2.49mm)

In the previous plot (Fig 7.16) and in the following tables 7.11 - 7.12 the results are shown. It is interesting to note that even in these results, the pattern found in the previous measurements is repeated, but the trend is the opposite way round; with a hot anode, the photon numbers decrease above 45 keV and increase below 45 keV. Changing the emission angle, there is a change in the spectra. In the chapter *processing data*, this situation will be simulated and will be confirmed. Another aspect to take into consideration in the behaviour of the effect and the trend is when the first collimator (C1) is increased in front of the window of the X-ray tube. As can be seen in the plot and in the table, the percentage of the effect is inversely proportional to the collimator (C1) diameter. These preliminary results (Fig 7.16) with the increased opening of the first collimator, could lead us to a conclusion: the "*hot-cold effect*" can be caused by irregularities on the anode surface, due to roughness and local bending. To check the nature of these results the following measurements were recorded, replacing the first collimator with filtered material. The main purpose of this last test, was to observe and analyse the behaviour of the whole beam, having eliminated selection due to the first collimator. In this way it was possible to have a better understanding of the "hot-cold effect" and find out if we were dealing with a local or non-local effect.

**Copper filtration** The first set of measurements in hot and cold conditions were recorded replacing the first collimator (C1) in front of the X-ray window, with a thin copper layer (2.49 mm).

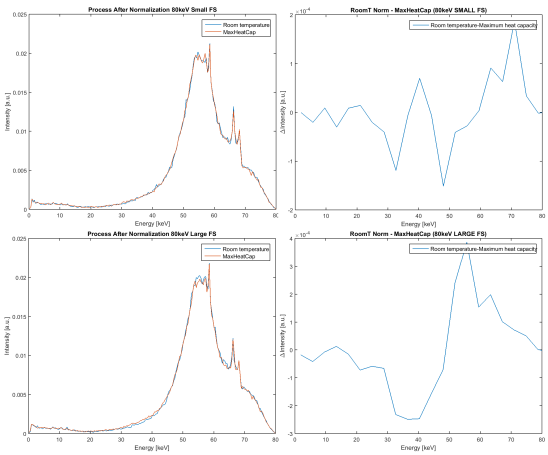


**Figure 7.17:** *Spectra recorded without the first collimator (C1, replaced by 2.49 mm of copper. Above the small focal spot and below the large one. The settings use for these measurements are 80 kV and 10 mA.).*

The results are shown in the plot below with the total counts in the table 7.12. As can be seen from the spectra, the copper filtration, due to photo electrical absorption, reduced the low energy spectra; for our studies, this can influence the results because the counts in the first bin (before 45 keV) are strongly reduced.

**Gadolinium filtration** The Gd was choose due to its property of having a k-edge at 50 keV, to better balance the source spectrum in favor of energies below 50 keV. One layer of gadolinium (0.5 mm) was ordered to replace the Cu.

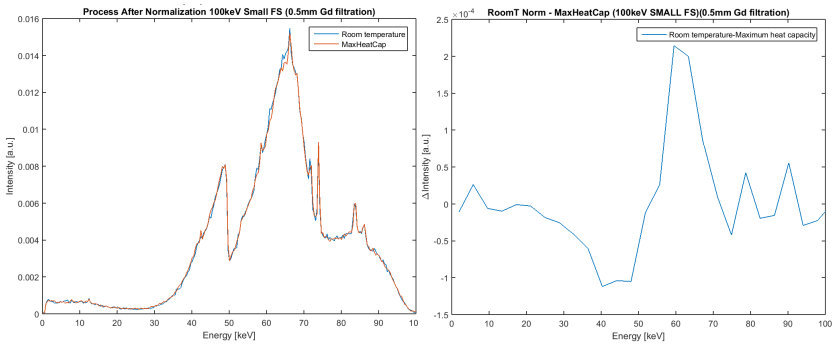


**Figure 7.18:** *Spectra recorded without the first collimator (C1, replaced by 0.5 mm of gadolinium. The settings use for these measurements are 100 kV and 10 mA and small focal spot).*

Above the results and the spectra recorded with gadolinium filtration are shown.

| **SMALL FOCAL SPOT (−7°)** | | | | | | | | | |
|---|---|---|---|---|---|---|---|---|---|
| | **10 mA** | | | | | | **40 mA** | | |
| | collimator 400$\mu$m | | | collimator 200$\mu$m | | | collimator 100$\mu$m | | |
| bin | cold % | warm % | Δ% | cold % | warm % | Δ% | cold % | warm % | Δ% |
| 0 | 0.6878 | 0.6875 | **0.03** | 0.6782 | 0.7032 | **-2.50** | 0.5813 | 0.6214 | **-4.01** |
| 1 | 0,2962 | 0,2972 | **-0.10** | 0,3105 | 0,2855 | **2.50** | 0,4083 | 0,3680 | **4,03** |
| counts | 355K | 327K | **28K** | 93K | 126K | **-33K** | 49K | 62K | **-13K** |

**Table 7.11:** *Differences due to the temperature for the different acquiring condition for the small focal spot.*

| | **Large FS (−7°)** | | | **Gd filtration (0.5mm)** | | | **Copper filtration (2.49mm)** | | |
|---|---|---|---|---|---|---|---|---|---|
| | **10 mA** | | | **10 mA** | | | **10 mA** | | |
| | collimator 400$\mu$m | | | No first collimator | | | no first collimator | | |
| bin | cold % | warm % | Δ% | cold % | warm % | Δ% | cold % | warm % | Δ% |
| 0 | 0.6943 | 0.7027 | **-0.84** | 0.2245 | 0.2293 | **-0.48** | 0.3483 | 0.3471 | **0.12** |
| 1 | 0,2958 | 0,2874 | **0.84** | 0,7280 | 0,7229 | **0.51** | 0,6213 | 0,6209 | **0.04** |
| counts | 82K | 83K | **-1K** | 440K | 442K | **-33K** | 109K | 109K | **0K** |

**Table 7.12:** *Differences due to the temperature for the different acquiring condition for the large focal spot and for the filtration.*

The previous hypothesis explained above regarding the increasing of the collimator C1 diameter, seems to have been confirmed. In fact, without the first collimator, the effect is decidedly less, but is still visible; the trend is always the same, but the intensity of the effect is one order of magnitude lower, as can be seen in the table.

## 7.3 Spatial Scanning

This last section shows the measurements taken while consistently shifting both collimators perpendicular to the optical axis. In this way X-ray spectra at different positions were acquired and consequently, it was possible to do a complete scanning of the areas of, the small and large focal spot. The purpose was to be able to see how the X-ray spectra changed on different point of the focal spot; the heel effect cannot contribute because a more or less fixed emission angle with respect to the anode surface was selected. The operating conditions were the same as those described in the previous paragraph 7.2.1: 100 kV, 10 mA and both collimators were simultaneously moved in the same direction and with same translation such that the optical axis defined by the collimator hole openings scanned across the focal spot area.

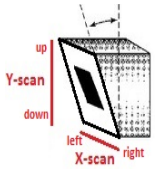


**Figure 7.19:** *X and Y scan of the focal spot.*

This allowed us to make a precise scanning and record all spectra generated. The following diagrams illustrate the spectra recorded during the scanning of the small focal spot along X and Y and then of the large focal spot. In the spectra shown below, the characteristic peaks have been omitted in order not to flatten the lower part of the graph. However, even just with the bremsstrahlung radiation, the differences in the graph, are visible.

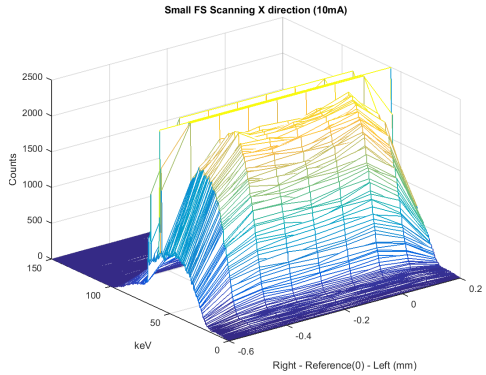


**(a)** *Small F.S.*

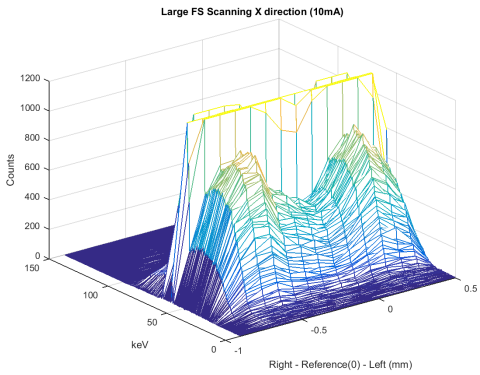


**(b)** *Large F.S.*

**Figure 7.20:** Scanning along the X direction.

Therefore the different intensity emitted by each point of the focal spot can be observed. As is explained in the documents included in section 5.2, the tube cathodes as electron emitters are two different coils and because of the mere presence of the cathode cup, different areas of the anode are involved.

This test was carry out for many different reasons: first of all, as already said in the previous chapter, the maximum emission point could be located and subsequently

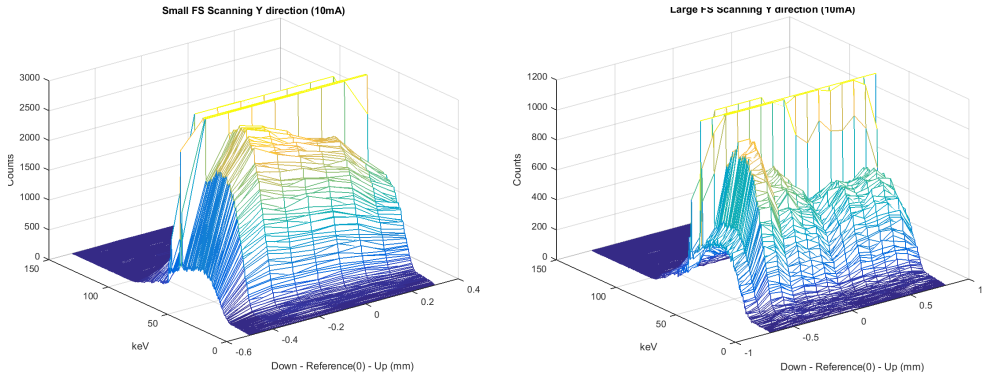


**(a)** *Small F.S.* **(b)** *Large F.S.*

**Figure 7.21:** Scanning along the Y direction.

the collimators could be placed in that position. Moreover with this type of testing it was possible to judge the condition of the anode and cathode by assessing the quality of the spectra recorded. The intensity profiles observed here are a consequence of the electron source profile and the electron lensing effects by the cap. In tendency this leads to intensity enhancements of the spot in the periphery (giving that typical "camel"-like profile shown in Fig.7.19b). In simple words, an "image" of the coil is generated within the focal spot area. For the application the profile doesn't matter much, although it does matter for the physics of heat deposition.

The same scanning process was repeated again, but with two differences: this time the collimators was moved 0.2 mm each time rather then 0.1 mm and testing was done at maximum tube temperature. This was done to compare the two different conditions and check if the hot cathode could alter the emission geometry (fig.7.22-7.23). The spectra were recorded for 40 seconds (but just 20 seconds of X-ray on, due to the pulses) with a 20 minute break between one recording and another to allow the tube cool down and reduce the temperature effects (even if with just 10 mA the changing in temperature is not substantial). Comparing these two patterns, it is possible to say that for the scan along the X direction, the position of the focal spot and consequently the pattern of the various spectra taken at different position, seems almost the same. On the contrary, for the Y direction there is quite an interesting change in the position of the anode focal spot. Looking to the fig.7.22 it's clear how the "image" of the focal spot is extended in the "up" direction. In fact it is possible to see how the cold spectra at 0.8mm is already weak, but the hot spectrum at 1mm is still intense. Excluding the effects caused by the electronic optics, the only two factors left to justify such a difference are the following: due to the heating of the anode, it is possible that the surface of the focal spot track changes the curvature and this leads to a changes in the X-ray angular emission. Obviously this could lead to a change in the focal spot "image" given by the spectra recorded; there might be an additional effect caused by the coil.

The distribution of the electron emission along the filament might not be uniform because of the uneven spatial distribution along the spiral coil, on comparing hot and cold conditions (depending on status of spiral coil).

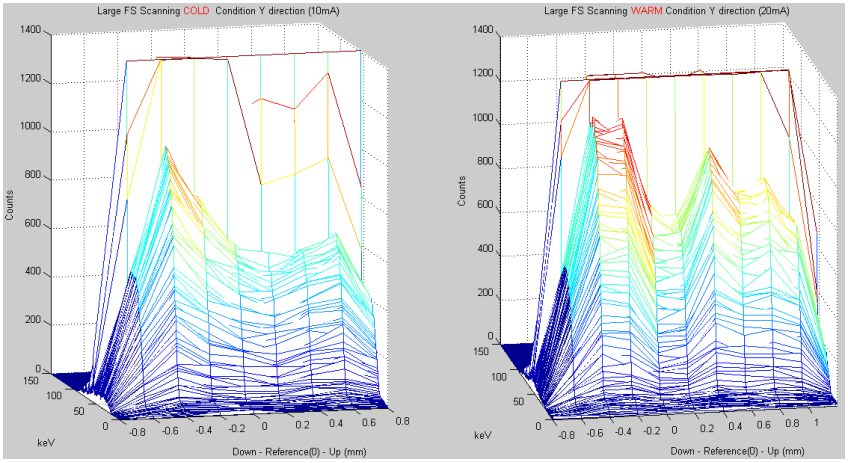


**Figure 7.22:** *Comparison between the hot and cold emission profile along Y.*

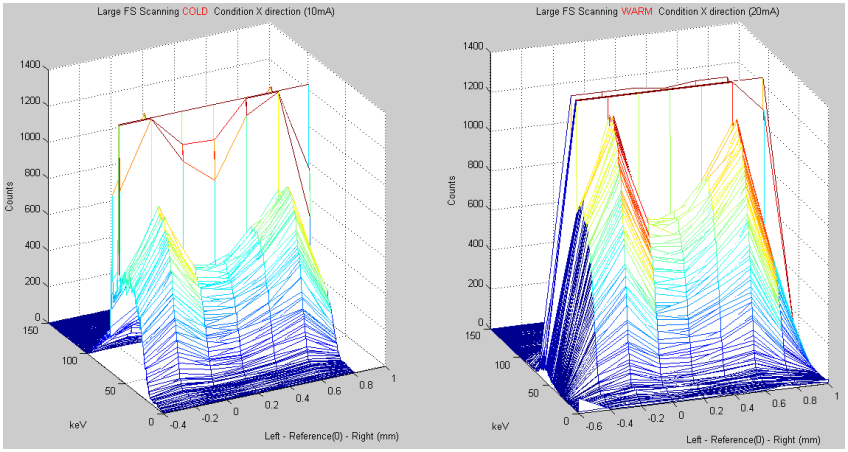


**Figure 7.23:** *Comparison between the hot and cold emission profile along X. "Left" "reference" and "right" mean the scan movement. Reference(0) is the position were the scan begin, left and right mean the shift of the collimator of 0.2mm along the left or right direction 7.19*

# Chapter 8

# Processing data and checking different assumptions

Here the various scenarios that can cause the difference between the spectrum recorded at room temperature and that one recorded with the hot anode seen in the chapter 7 will be analyzed. While attempting to fully understand every reasons that cause that behavior, in order to try to include them in the simulations in a proper way. After this operation it will be possible to improve the prediction of the spectra and simulate in a more precise way differents kind of situations. Below is a list of all the effects that can cause the behaviour explained in the previous chapter 7:

1. optical component and e-beam movement due to electronic focusing (same part on the anode but different angular incidence, that could influence the spectra);
2. keV ripple;
3. density change (anode and filtration material)
4. Anode ageing: wrecked anode – rough surface → mix of different angles distribution and different self absorption due to cracks (attempt to simulate this condition);
5. anode bowing - potential change of surface geometry to more curved structure - also at different angles distribution - will probably reduce the effect of cracks due to "closing of cracks";
6. the spatial distribution along the spiral coil of the electron emission might be different in hot and cold condition.

## 8.1 Electron optics

The first thing that it is possible to do, supplied by the tube manufactures (fig.5.4), is to discard the fourth hypothesis. From the documentation, the position of the small focal spot and the large focal spot are slightly overlap but they come from two different emitter positions without electronic focusing. So, in the tube used in this experiment, there isn't a big focusing unit, just a small cathode cup that couldn't affect in a significant way the spectrum obtained. For this reason, the expectation is

that the main part of the hot and cold anode effect will come from the emitter and focal shape on the anode and not from the optical component and focusing unit.

## 8.2 High Voltage generator

In this section the generator effect will be studied to see if any change in behaviour occur in hot and cold condition. Anyway the expectation is, as shown in the table 7.9-7.10 that the hot and cold effect is still visible on different mA, so, even if there is a small generator effect, it won't be the main cause. This type of check was carried out, because during the time in which the tube is brought to high temperatures it were used high mA and high kV, and it was necessary to be sure that in this interval time, no changes occurred to the high voltage generator, or to its electronics occurred. To this kinds of measurements an oscilloscope was connected to the control output of the HV Generator and the AC (alternating current) and DC (direct current) voltage were analysed as can be seen below. This type of analysis was done using the properties of the oscilloscope to record 3 different signal: the AC DC voltage and the fourier transform to analyse the frequency. A normal recording with the X-ray tube was done and during this measurement the signals mentioned above, were acquired. At the same time, the cold spectra and the voltage under the same condition were recorded, and later, after heating the tube the acquisitions were repeated.

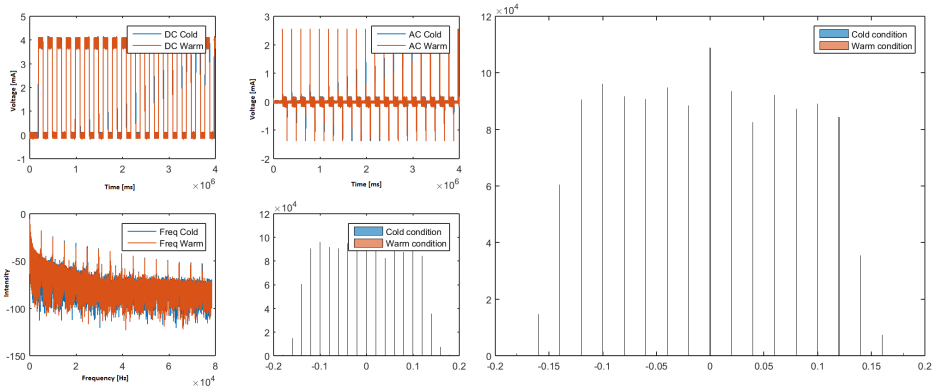


**Figure 8.1:** *Comparison of AC, DC and frequency of AC signal in hot and cold conditions.*

| | Mean Peak (+) | Mean Peak (-) | Mean | Area |
|---|---|---|---|---|
| Cold | 0.1545 | -0.1618 | -0.0054 | $9 \cdot 10^4$ |
| Hot | 0.1553 | -0.1622 | -0.0051 | $9 \cdot 10^4$ |

**Table 8.1:** *Mean peak (+ -) and mean of AC voltage for two different condition: hot and cold. "Area" is the area under the curve of the AC signal.*

Obviously the pulses shown are not comparable with the pulses that reaches the X-ray tube, since the check output of the generator from which are picked up the mentioned signals, was positioned before all the electronics that modify the input signal in the tube. But this does not jeopardise analysis or control, because if some

signal changes happened, these would be visible even from the check output of the generator. The point of interest here is not the absolute signal, but the differences related to the two different condition. The simultaneously acquired spectra show the same characteristics as reported in fig.7.12 of section 7.2.1. Regarding the HV, a numerical analysis done in the table 8.1 and a graphical analysis in fig.8.1 was carried out in order to have the greatest possible number of parameters (mean peak and mean AC, histogram, fourier analysis) to compare. The values in the table 8.1 refer to the the AC voltage, instead, for the image, the comparison were with the AC, DC and the frequency spectrum, given by the oscilloscope. As can be seen from the table and the images, there is no differences at all, so the hypothesis that the generator could influence the obtained result, can be completely discard.

## 8.3 Density change

Of course the mass density of the anode changes during the heating up and cooling down process, but when this happens the electron penetration depth changes; if the density decreases the electrons can go deeper into the target, according to the law shown in the equation 8.1.

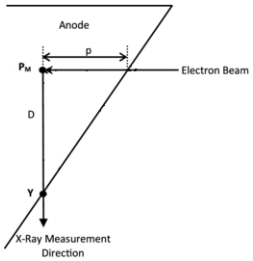


**Figure 8.2:** *During a density change "p" change and consequentially also "D" change in order to compensate the change of "p".*

The electron penetration depth is inversely proportional to density changes and the X-ray filtration is proportional to $-\mu \cdot \rho \cdot x$; so what happens is that if the electron goes deeper due to density changes, the X-rays comes out with more target material. So whatever effect you have, because of the density change, they cancel each other.

$$AverageRange(cm) = \frac{1}{AttenuationCoefficient(cm^{-1})} \tag{8.1}$$

## 8.4 Simulation

After having analysed and rejected the less likely hypothesis, the next step is to focus attention on what conceivably could be the causes of the hot and cold effect. The only thing that remains to be examined is roughness and bending-bowing. Simulation using the Philips software described in chapter 4 was used to try and differentiate between these two effects and study them in detail. In this way it was possible to change parameters such as tungsten filtration (a different level of roughness causes a different degree of filtration) and the emission angle that varies as a function of anode bending and bowing.

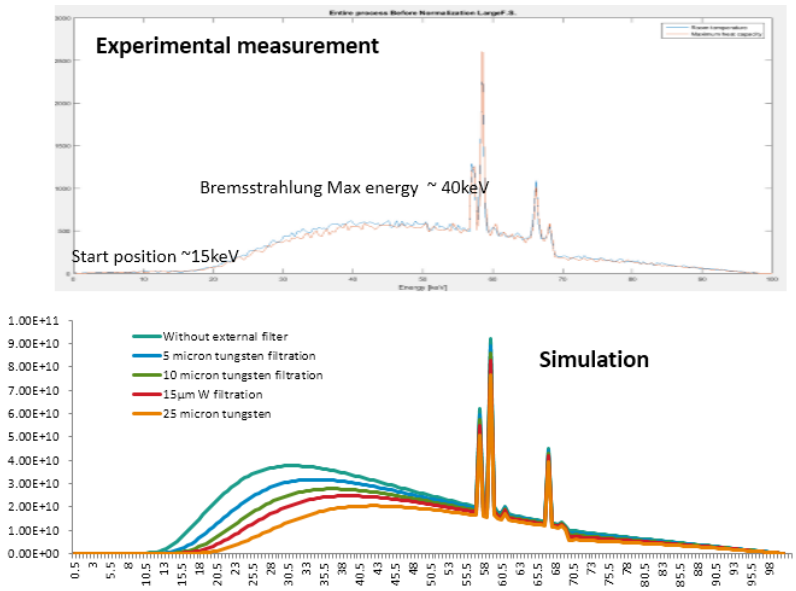


**Figure 8.3:** *On the left side the experimental spectrum, on the right side different simulated spectra with different tungsten filtration.*

The first thing that emerged from simulations is that the spectrum achieved initially through experiments has a different filtration. This is evident from the more pronounced drop down after the characteristic peaks and maximum energy of the bremsstrahlung spectrum shifted to 40 keV. To match the simulated spectrum with that one obtained in the laboratory was necessary to add 20$\mu$m of tungsten filtration, as can be seen even in the simulation below. There are essentially two reasons: the roughness of the anode and the possibility that the collimators are not perfectly aligned, and in this case there is some additional tungsten filtration along the beam path. It is possible to straight reject the second hypothesis because if that happens, the additional tungsten should be much more than a few $\mu$m, so this thesis is not very plausible.

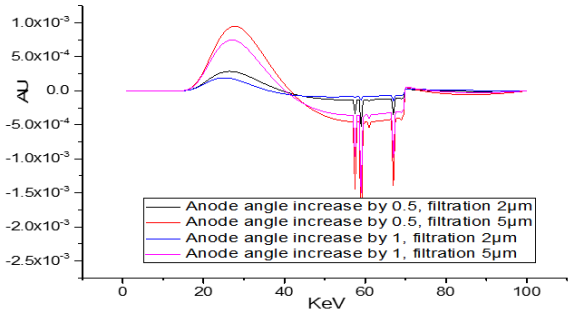


**Figure 8.4:** *The difference between two simulated spectra with different angular emission (due to banding) and different filtration (roughness).*

Once the two spectra were matched (simulated and experimental) $\mu$m of tungsten filtration and angular emission were varied in order to try to simulate the behaviour and the trend of the difference between the spectrum achieved in hot and cold conditions.

The first result was that, it proved impossible to simulate this effect by introducing just one of these factors between roughness (changing tungsten filtration) and bowing (changing the emission angle); therefore, at least from the simulations, it seems that the effect is caused by both factors. The following simulation demonstrated the same trend found in chapter 7.2, apart from the presence of the characteristic peaks. So, on the basis of these simulations, the effect of additional filtration and different angular emission will be separately analyzed in the following chapter which will attempt to explain how these two effects may influence the outcoming spectra during the heating of the tube.

Another kind of simulation was done to check the different emission angle; as it can be seen in "hot and cold measurements" chapter 7.2, changing the set-up configuration in section 7.2.2, means change the emission angle. Consequently, as it can be seen in the previous results, this affect the effect trend. Therefore the idea was to simulate this changing in the emission angle and check if the simulation can match the experimental results.

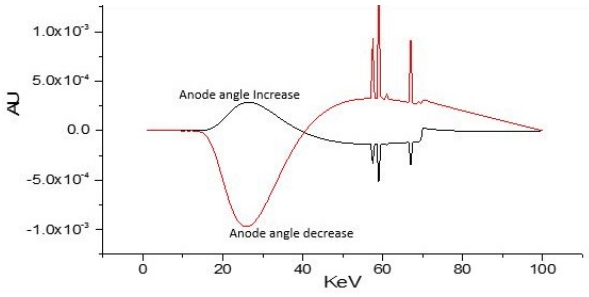


**Figure 8.5:** *The difference between the the two spectra (hot and cold condition); the red one, is the one with the second configuration with the angular emission* $= -7°$.

As it can be seen in the plot above, changing the angular emission from $0°$ to $-7°$, the trend change and become the opposite; according with the experimental results obtained in the the previous chapters.

## 8.5 Anode configuration

X-ray spectra produced with X-ray tubes depend primarily on tube voltage and voltage ripple but these are not only the parameters that can influence the outgoing spectra. In diagnostic units, some minimum photon attenuation by the absorbing materials between the anode and beam exit is mandatory to reduce the radiation dose to the patient from the low energy X-rays in the spectrum. Some additional filters are introduced to achieve a filtration of an equivalent in aluminium of typically 2.5 mm. In therapy and metrology various filter combinations are used to achieve the radiation qualities required. In addition, the attenuation of the X-rays in the anode material itself, its bending and bowing and emission angle (self absorption of the anode) also contributes to filtration. The X-rays produced by electrons slowed down in the anode encounter some attenuation in the anode material depending on the anode angle and the beam direction. The purpose of the following paragraph is to analyse both the roughness and the bowing of the anode itself. Here the main causes of these two effects will be analysed taking into account that lack of information will make this analysis

more difficult. Not much information is available about these new aspects. They are new aspects with not so many informations, especially in these operating conditions.

### Optical profilometry

Another way to analyse and try to reach some conclusion on the hot and cold effect was the optical profilometry of the anode (new vs aged). As it can be seen in fig.8.6, the two anodes and the two tubes have different configuration and here, the effect could be magnified by the absence of the slits in the anode, that can reduce the banding of the anode during the heating. At the same time in a CT tube the heat and the power load on the anode are significantly stronger.

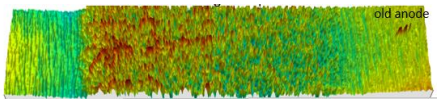


**(a)** *Optical profilometry and SEM for SRM tube.*

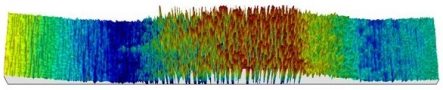

**(b)** *Optical profilometry and SEM for CT tube anode.*

**(c)** *SRM anode (picture).*


**(d)** *CT anode (picture).*

**Figure 8.6:** Difference between the two different anode. The different roughness profile in the two different kind of anode and different structure are shown.

This SEM result could also be the reason what provoked the effect, because a small bending of the anode due to the temperature, can cause a change in the spot position on the anode and then a different area with a different roughness could be lit up.

### Bowing and bending

As regards the bowing and the bending of the anode, some studies has been carried out in the past, but just by comparing the new anodes with the old ones; the effects that become evident through this comparison are called "long term effect".

**Figure 8.7:** *In a new anode the light shouldn't go through the bar in the focal tracks. Here, in both tracks a kind of bending is visible that allows light to pass.*

In the Fig.8.7 some bending is visible on an old anode. With anode ageing there is a change in the emission angle due to this local bending and bowing, but it is still unknown how this behaves at higher temperatures. However, if there is a change in the effective angle distribution, the effect on the spectra can be indicated by simulation.

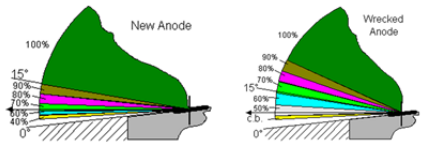


**Figure 8.8:** *The images represent the difference in the emission angle caused by the bowing due to ageing. In an wrecked anode the emission angle with less intensity than 100% is consistently wider than in the new one and the opening of the maximum intensity emission angle is noticeably reduced in the wrecked anode. Surely this kind of bowing also occurs during heating and cooling, but at present, how and to which degree that happens, is still unknown [From Philips GTC- C. Bathe].*

During the acquisition, there are some effects, like the opening or the closing of the cracks and bending that can influence the X-ray beam, due to the heating up and cooling down; these effects are called "short term effects". The difficulty in explaining this type of effect is in simulating the operating conditions inside the tube with the temperatures reached by the anode. Some simulations of these effects were done [21] and in the following Fig 8.9 there is the explanation of how the rise in temperature can lead to an expansion of the anode. Naturally this expansion is greater in anodes without slits. Instead in CT tubes there are slits in order to avoid this type of effect and bowing. The expansion of the anode could cause a shift of the track and a consequent change in the output spectrum.

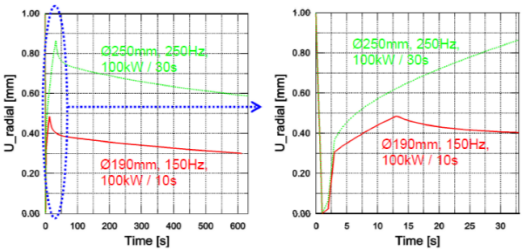


**Figure 8.9:** *Explanation of the anode extension as a function of applied power and time. Evolution of the displacement at the outer diameter of targets d=190 and d=250 for load of 100kW / 10s / 150Hz and 100kW / 30s / 250Hz.*

There is no doubt that the above-mentioned effects exist, but as yet their real influence on the spectrum is unknown. However from the results obtain from this work, it is certain that they play an important role. The next step is to quantify these effects to be able to model and include them in the simulation models.

### Roughness

The condition of the anode surface and the deposition of sputtered tungsten on the tube envelope have also been made responsible for an increased effective inherent filtration (see e.g. Ardran and Crooks (1972)).The anode aspects definitely influence

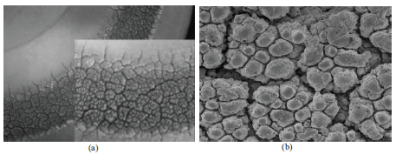

**(a)** *(a) A digital image taken from an old anode disk and a close-up of its focal path surface. (b) An SEM image from the central part of the focal path in (a) with a magnification of 30*[1].

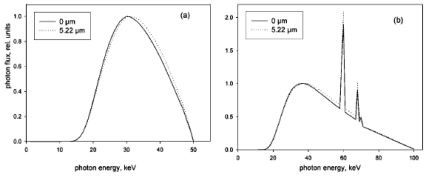


**(b)** *X-ray spectra for a plain anode and an anode with a roughness of 5.22 µm normalized to the maximum of the bremsstrahlung distribution calculated for tube voltage (a)50 kV (b)100 kV*[1].

most the way in which the spectrum is emitted. Below there are some analysis and studies [18] which confirm how 5-15 $\mu m$ of anode roughness can substantially affect and modify the path of the electrons, and subsequently the X-ray beam output.

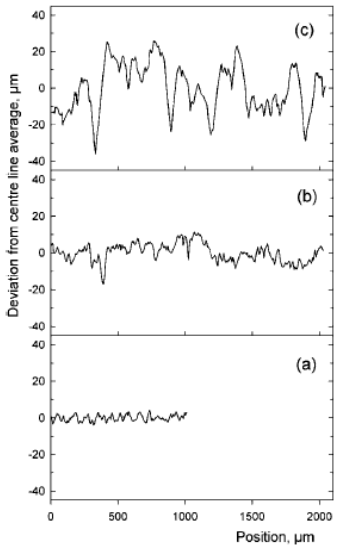


**Figure 8.10:** *Surface profiles for an anode from a diagnostic X-ray tube measured with a stylus method. Data shows the deviation from a centreline versus position for (a) the original anode surface (ground surface finish), (b) the surface of the large focal track and (c) the small focal track. All scans were taken on the anode disc in a radial direction[18].*

As these studies suggest, the effect of roughness is definitely present; unfortunately even here, as previously, there are studies that analyze only the "long term" effect and not the "short term" which are created inside the tube due to thermal stress. it is therefore possible to conclude that, if an old anode has these furrows, cracks and tunnels, surely with heating, there will be structural changes. This leads the study to assert, based on the differences found between an old and new anode, that the effects of hot and cold shown above, can be result in roughness change of the anode surface. Obviously, for now, it's still impossible to know which of the two effects, this and anode bowing, contribute the most and how, but future studies will lead to an answer to this question. Furthermore, on the basis of different results achieved with

different collimators and filter material, it is still impossible to affirm the source of this effect; whether this is a strictly local behaviour and is mediated in an approach without collimators, or if this behaviour is still present without collimators and has to be considered in any case.

# Appendix A

# Cooling and Heating chart

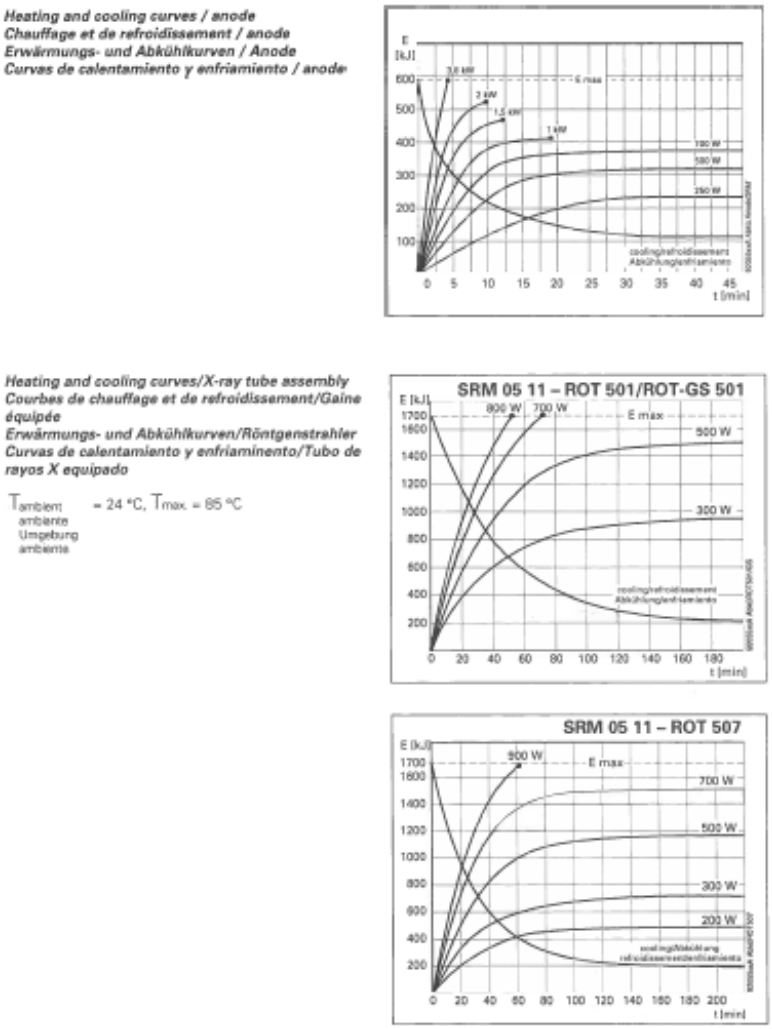


**Figure A.1:** *Cooling and Heating chart for the SRM Philips tube.*

# Conclusions and future applications

The main goal of this study was the investigation of the stability of the X-ray spectrum generated by a Philips SRM (Super Rotalix Metal) X-ray tube for cardiovascular applications in order to obtain precise information about the reasons and measurements of the time dependent changes are prerequisites for improved quantitative performance. Calibration and correction methods could be applied if the influence of the changes in the tube spectrum is large enough for the final outcome. As energy resolved X-ray imaging in the new modality of spectral CT requires exact understanding of the spectral performance these investigations are useful for an overall performance and risk analysis. An old tube with aged anode was used; this choice was made in order to analyse the stability and the reliability of the spectra emitted in a realistic (i.e. typical) usage case because this is one of the most important aspects to check in a spectral CT scan. A portable set-up was built and the first measurements to check the stability of the whole system were recorded. During checking, a particular trend in the measurements recorded during hot and cold condition was detected. The differences which became apparent from the experiments are are significant, because the percentage of the difference of the hot and cold spectra in tab. 7.10-7.9 is always between 1.5% and 2.5%, whereas overall intensity changes of less than 1% have effects on the image quality; the 1.5% of spectrum change do not necessarily have as a consequence also a 1% change in the overall intensity but other effects (detector, ...) have also to be considered. The results, also show how the trend is similar for different focal spots sizes and positions. However these deviations become reduced to 0.5% (tab.7.11-7.12) while opening the collimator at the tube window side. In this case, the percentage goes down, and this could lead us to the hypothesis of a local-effect due to roughness and bending. Further examinations included:

- simulation tools (8.4)
- optical profilometry and SEM of the anode (8.5)

An attempt was made to simulate these results with the Philips simulation tool, in order to check the hypotheses of roughness (different tungsten filtration) and anode bending (change in angular emission). Simulation results point to increased anode angle and filtration during heating as a plausible explanations of the effect. Furthermore, the SRM anode targets were investigated by optical profilometry and SEM, and the results show the target with two distinct roughness profiles. This last result could also be the reason what provoked the effect, because a small bending of the anode due to the temperature, can cause a change in the spot position on the anode and then a

different area with a different roughness could be lit up. All these factors listed above were found in an SRM tube analysis. These effects are measured at an aged anode as a kind of worst case condition. The performance of a CT tube might differ due to several additional components that have influence on the X-ray generation. One aspect to take into account is the absence, in the SRM tube, of the quadrupole for the electron optics inside the housing; for the spectral CT scan, there are three main aspects to take into consideration:

- different focal spot shape (cathode): double filament for SRM tube and flat emitter for CT tube;
- different collimation in CT, both are more or less "cone beams" but CT collimation is of course not comparable to the collimator set-up used in the experiments;
- the generator, filament and the tube is heated up.

The spectral CT beam is strongly filtered in order to remove the low energy spectrum, which is useless for the image and this mean that the effect recorded in this work, could be interesting just for the second part of the spectral distribution (after 45 keV). It is also worth noticing that, assumed is used to cut the spectrum at 40 keV, the normalization procedure will modify the difference spectrum such that a complete new "trend" will be see. I.e., the "zero" in the difference function will shift towards higher energies, and a redefinition of the energy binning is needed. The other interesting aspect, is that the beam during the exams is not collimated. In the CT case an average is received over the whole focal spot, which of course include an average over different emission angles. If selecting only a small area by collimator, only roughness and bending of that small region are seen, for which experiments indicated much higher instability. Therefore, if the according spectra from the areas are unstable in their sum, having different emission from different part of the anode (local-effect) during hot and cold condition can cause issues in the image reconstruction process. On the contrary it is also possible to have the effect that the local spectrum deviations cancel each other in the sum, so the CT spectrum from the whole spot becomes more stable than that from small areas. The last difference between this current experiment and a normal CT scan is the starting tube temperature, the power loading and the different cooling period. In a normal scan the initial condition of the electronics and electron emitter are not completely cold. The tube anode is not heated, has active cooling and so it might become cool (depending on the time since the last scan). All these factors are to take into account in order to calculate the percentage effect that should be less because the gap between hot and cold condition will not be same. In this experiment the measurements were recorded with the cold tube, and with the 80% of maximum heat capacity (hot condition), on the contrary in a CT scan, the starting record is not taken in a completely cold condition.

Therefore the ideas for the next experiment and the future application are to repeat the experiment with a CT tube, to search for similar spectral shift due to anode temperature and other potential effect relevant to spectral CT; like above and with typical CT filtering, standby temperature, and protocol (power load, pauses). As shown in the profile in fig.8.6 (paragraph 8.5) DMRC anodes of different lifetime are under investigation to check the surface roughness, crack depth etc. Based on the above outcome, it is planned to simulate the effects of roughness with respect to the spectrum. Moreover simulate and try to estimate with experiment the anode bending,

the expansion in short term and the expansion/contraction of grains and slits, due to the heating of the tube. A future continuation of this work it will be to ensure that this effect could be interesting for the spectra CT application and after that, find a way to model this behaviour and simulate in order to have a perfect knowledge of the outgoing spectrum stability.

# Bibliography


[1] N. Riyahi Alam and H. Zaidi. "Quantitative assessment of the Effect of Anode Surface Roughness on Diagnostic X-ray Spectra: A Monte Carlo Simulation Study." In: *IEEE* (2009).

[2] Alvarez. "Near optimal energy selective x-ray imaging system performance with simple detectors." In: *Med.Phys.* (2010).

[3] *Amptek collimator kit*. 2002. URL: http://www.amptek.com/pdf/collkit.pdf.

[4] Ardran and Crooks. "The measurement of inherent filtration in diagnostic x-ray tubes and the effect of target angle on x-ray quality." In: *Br. J. Radiol.* (1972).

[5] A.S.Wang and N.J.Pelc. "Sufficient statistics as a generalization of binning in spectral X-ray imaging." In: *IEEE Trans. Nucl. Sci.* (2010).

[6] Birch and Marshall. "Computation of bremsstrahlung X-ray spectra and comparison with spectra measured with a Ge(Li) detector." In: *Phys. Med. Biol.* (1979).

[7] Bushberg et al. *The essential physics of medical imaging*. 2001.

[8] *Canberra datasheet*. 2012. URL: http://www.canberra.com/products/detectors/pdf/Low-Energy-Germ-C39331.pdf.

[9] Nagel H. D. "Limitations in the determination of total filtration of x-ray tube assemblies." In: *Phys. Med. Biol.* (1988).

[10] Epp and Weiss. "Experimental study of the photon energy spectrum of primary diagnostic x-rays". In: *Phys. Med. Biol.* (1966).

[11] E.Roessl and R.Proksa. "K-edge imaging in x-ray computed tomography using multi-bin photon counting detectors." In: *Phys. Med. Biol.* (2007).

[12] Stears J. G., Felmlee J. P., and Gray J. E. "Half-value-layer increase owing to tungsten buildup in the x-ray tube." In: *Radiology* (1986).

[13] Hendee and Ritenour. *Medical imaging physics*. 2002.

[14] J.E.Daniels and M.Drakopoulos. "High-energy X-ray diffraction using the Pixium 4700 flat-panel detector." In: *European Synchrotron Radiation Facility* (2009).

[15] J.P.Schlomka et al. "Experimental feasibility of multi-energy photon-counting K-edge imaging in pre-clinical computed tomography." In: *Phys. Med. Biol.* (2008).

[16] J.S.Iwanczyk et al. "Photon counting energy dispersive detector arrays for x-ray imaging." In: *IEEE Trans. Nucl. Sci.* (2009).

[17] Kramersh. "46, 836." In: *Phil. Mag.* (1923).

[18] Nowotny and Meghzifene. “Simulation of the effect of anode surface roughness on diagnostic x-ray spectra”. In: *Phys. Med. Biol.* (2002).

[19] L. H. J. Peaple and A. K. Burt. “The Measurement of Spectra from X-Ray Machines”. In: *Phys. Med. Biol.* (1968).

[20] P.Fischer et al. “Single Photon Counting X-ray Imaging with Si and CdTe.” In: *IEEE Trans. Nucl. Sci.* (2000).

[21] Arno Plankensteiner and Peter Rödhammer. *Finite Element Analysis of X-Ray Targets.* 2000.

[22] Rao-Sahib and Wittry. “45, 5060-5068.” In: *J. Appl. Phys.* (1974).

[23] Reed. “4, 14-17.” In: *X-ray Spect.* (1975).

[24] Ewald Roessl et al. “Preclinical spectral computed tomography of gold nanoparticles.” In: *Nuclear Instruments and Methods in Physics Research* (2010).

[25] Soole. “22, 187-207.” In: *Phys. Med. Biol.* (1977).

[26] Soole. “5, 1583-1595.” In: *J. Phys. B: A tom. molec. Phys.* (1972).

[27] Tucker, Barnes, and Chakraborty. “Semiempirical model for generating tungsten target X-ray specra”. In: *Med. Phys.* (1990).

[28] Wang et al. “Pulse pileup statistics for energy discriminating photon counting x-ray detectors.” In: *Med. Phys.* 38 (2011), p. 4265.

# Declaration

This thesis is a presentation of my original research work. Wherever contributions of others are involved, every effort is made to indicate this clearly, with due reference to the literature, and acknowledgement of collaborative research and discussions.

The work was done under the guidance of Dr. Gereon Vogtmeier, Dr. Klaus-Juergen Engel, at the High Tech Campus Philips Research, Eindhoven.

*Bologna, March 11, 2016*

Riccardo Baldoni

*There isn't a better moment than this to be happy.*
*Happiness is a path, not a destination.*
*Work as if you didn't need money, love as if no one ever hurt you*
*and dance, as if no one saw you.*
*[...]Behind every goal is a new start.*
*Behind every result is a new challenge. While you're alive, feel alive.*
*Go on, even when everyone expects you to give up.*

— Mother Teresa

# Acknowledgments

First of all I would like to thank my supervisors Gereon and Klaus Juergen who have given me the chance of having this brilliant experience. I really appreciate their precious time and the passion they had with me over the entire year of work. I am also grateful for the passion and the interest they transmitted to me. In addition I would also like to thank Professor Baldazzi who despite his many commitments and the distance that separated us, always managed to give me valuable advice.

Ringrazio tutti gli amici sinceri che mi sono stati vicino in questo percorso e sono riusciti a supportarmi durante le difficoltà.
Riccardo che dopo 20 anni è ancora qui a sostenermi come solo i veri amici sanno fare, come se ci conoscessimo da ieri, a consigliarmi nei momenti difficili e non si è ancora stancato di me.
Diego e Gianluca che nonostante la lontananza ed i problemi nel riuscire a vedersi, hanno sempre trovato il modo di aiutarmi e farmi sfogare e si sono sempre fatti trovare pronti nei momenti in cui avevo bisogno.
Ringrazio Pierfrancesco che nonostante ci conosciamo da anni, ci siamo riscoperti negli ultimi mesi ed è stato fondamentale per aiutarmi a superare gli ultimi ostacoli e le ultime difficoltà per il raggiungimento di questo obiettivo.
Vi ringrazio per avermi sempre detto la verità anche quando era scomoda; questa per me è la vera amicizia.

Grazie agli amici di sempre come Gloria, Federico, Lorenzo e Andrea che anche con un messaggio ogni tanto, mi hanno sempre dato il loro appoggio.
Grazie a chi è entrato a far parte della mia vita in punta di piedi e nonostante mi abbia accompagnato nel mio percorso per poco tempo, mi ha aiutato nei mesi più difficili senza che nulla le fosse richiesto.
Finally thanks to all the people that I met during this experience who became part of my life for just a few months, but who treated me as if we had always been friends, especially Gerogy and Bero.

Concludo ringraziando soprattutto mia madre e mio padre che mi hanno sempre trasmesso sicurezza, calore e non mi hanno mai lasciato solo. La mia famiglia che mi è sempre stata vicino in ogni difficoltà e non mi ha mai fatto mancare il sostegno economico e soprattutto morale, permettendomi di raggiungere il traguardo più importante della mia vita. Ringrazio mio fratello che, forse inconsapevolmente, è riuscito a starmi vicino più di quanto lui possa immaginare. Grazie.

*Bologna, March 11, 2016* R. B.